Article

SOURCE DATA | TRANSPARENT PROCESS | OPEN ACCESS | CHECK FOR UPDATES

EMBO reports

Lack of p38 activation in T cells increases IL-35 and protects against obesity by promoting thermogenesis

Ivana Nikolic[1,8]✉, Irene Ruiz-Garrido[1,8], María Crespo[1], Rafael Romero-Becerra[1], Luis Leiva-Vega[1,2], Alfonso Mora[1,2], Marta León[1], Elena Rodríguez[1,2], Magdalena Leiva[1,3], Ana Belén Plata-Gómez[2], Maria Beatriz Alvarez Flores[1], Jorge L Torres[4,5], Lourdes Hernández-Cosido[6], Juan Antonio López[1,7], Jesús Vázquez[1,7], Alejo Efeyan[2], Pilar Martin[1,7], Miguel Marcos[4] & Guadalupe Sabio[1,2]✉

Abstract

Obesity is characterized by low-grade inflammation, energy imbalance and impaired thermogenesis. The role of regulatory T cells (Treg) in inflammation-mediated maladaptive thermogenesis is not well established. Here, we find that the p38 pathway is a key regulator of T cell-mediated adipose tissue (AT) inflammation and browning. Mice with T cells specifically lacking the p38 activators MKK3/6 are protected against diet-induced obesity, leading to an improved metabolic profile, increased browning, and enhanced thermogenesis. We identify IL-35 as a driver of adipocyte thermogenic program through the ATF2/UCP1/FGF21 pathway. IL-35 limits CD8⁺ T cell infiltration and inflammation in AT. Interestingly, we find that IL-35 levels are reduced in visceral fat from obese patients. Mechanistically, we demonstrate that p38 controls the expression of IL-35 in human and mouse Treg cells through mTOR pathway activation. Our findings highlight p38 signaling as a molecular orchestrator of AT T cell accumulation and function.

Keywords Adipose Tissue; Obesity; p38 Stress Kinases; Thermogenesis; T Regulatory Cells
Subject Categories Immunology; Metabolism; Signal Transduction
https://doi.org/10.1038/s44319-024-00149-y
Received 11 January 2024; Revised 15 April 2024; Accepted 17 April 2024
Published online: 10 May 2024

Introduction

Obesity is a serious worldwide health epidemic associated with an increased risk of life-threatening diseases (type 2 diabetes—T2D, cardiovascular diseases, and cancer) (Nikolic et al, 2020). The hallmark of obesity is a chronic low-grade inflammation, both systemically and in adipose tissue (AT). This inflammation is one of the main promoters of insulin resistance and the development of T2D (Saltiel and Olefsky, 2017). Inflammatory myeloid cells, including macrophages and neutrophils, are key players in obesity-related comorbidities such as diabetes and steatosis (Crespo et al, 2020; Gonzalez-Teran et al, 2016b). Chronic inflammation in obese AT is also mediated by adaptive immune cells, including $CD8^+$ and $CD4^+$ T cells (Schipper et al, 2012), and absence of these conventional T cells in mice reduces AT inflammation (Khan et al, 2014). $CD8^+$ T cell infiltration and accumulation in AT plays a crucial role in the recruitment of macrophages and the maintenance of inflammation (Nishimura et al, 2009). Single-cell RNA sequencing (scRNA-seq) of AT obtained from obese patients identified a potentially dysfunctional population of $CD8^+$ T cells associated with metabolic disease (Vijay et al, 2020). Moreover, whereas infiltration of AT by conventional T cells increases during obesity, the numbers of protective T regulatory (Treg) cells are sharply decreased, and expansion of this population ameliorates AT inflammation and insulin resistance (Ilan et al, 2010; Li et al, 2021). Tregs are abundant in lean AT from mice and humans, and levels of the Treg hallmark transcription factor Foxp3 show an inverse correlation with body mass index (Feuerer et al, 2009). This suggests that preserving Treg accumulation in AT could be a novel anti-obesogenic strategy.

In addition to controlling the immune response within AT, immune cells play a significant role in regulating AT thermogenic function. The recruitment of anti-inflammatory macrophages and type 2 innate lymphoid cells actively promotes adaptive thermogenesis (Cereijo et al, 2018; Lee et al, 2015), while pro-inflammatory macrophages and $CD8^+$ T cells are one of the main promoters of the compromised thermogenic capacity of AT (Moysidou et al, 2018; Sakamoto et al, 2016). However, the specific role of Treg cells in thermogenesis remains unclear, with some data indicating that this cell population facilitates obesity development and represses AT browning (Beppu et al, 2021), while other studies highlight the protective role of Treg cells in promoting adaptive thermogenesis and browning (Fang et al, 2020; Kalin et al, 2017). Further research in this field is necessary to gain a comprehensive understanding of

[1]Centro Nacional de Investigaciones Cardiovasculares (CNIC), Madrid 28029, Spain. [2]Programme of Molecular Oncology, Spanish National Cancer Research Center (CNIO), Madrid 28029, Spain. [3]Department of Immunology, School of Medicine, Universidad Complutense de Madrid, Madrid 28040, Spain. [4]Department of Internal Medicine, University Hospital of Salamanca-IBSAL, Department of Medicine, University of Salamanca, Salamanca 37007, Spain. [5]Complejo Asistencial de Zamora, Zamora 49022, Spain. [6]Bariatric Surgery Unit, Department of General Surgery, University Hospital of Salamanca, Department of Surgery, University of Salamanca, Salamanca 37007, Spain. [7]CIBER de Enfermedades Cardiovasculares, Madrid 28029, Spain. [8]These authors contributed equally: Ivana Nikolic, Irene Ruiz-Garrido. ✉E-mail: inikolic@cnic.es; gsabio@cnio.es

how Treg cells influence thermogenic mechanisms. Such insights could provide valuable information regarding the development of obesity and potential therapeutic strategies targeting AT metabolism.

The p38 kinases, comprising four members (p38α, p38β, p38γ, and p38δ), belong to the stress protein kinase family and are activated by the upstream MAP kinase kinases MKK3 and MKK6 (Gonzalez-Teran et al, 2013). The p38 pathway serves as a central regulator of the immune response and plays a critical role in the development of inflammatory diseases associated with obesity, becoming activated in various organs, including immune cells (Nikolic et al, 2020). For instance, the activation of p38γ/δ in neutrophils and p38α in macrophages promotes liver steatosis (Gonzalez-Teran et al, 2016b; Zhang et al, 2019). Interestingly, Treg cells present marked activation of the p38 pathway compared with conventional T cells (Huber et al, 2008), and the lack of p38α/β in T cells enhances Treg cell induction in mice (Hayakawa et al, 2017). Therefore, we wondered how p38 activation in T cells would affect AT inflammation and function during obesity. To address this question, we generated mice with specific deletion of the p38 family upstream activators MKK3 and MKK6 in conventional T cells (MKK3/6$^{CD4\text{-}KO}$ mice). In our study, we observed that the lack of p38 activators results in an increased population of Treg cells in circulation, lymph nodes, and AT in obesity. Furthermore, we described a novel function of p38 kinases in Treg cells: repressing IL-35 expression in human and mouse Treg cells through mTOR pathway inhibition. IL-35 levels, which are reduced in visceral fat from obese patients, directly correlate with reduced CD8$^+$ T cell infiltration and inflammation in AT. In addition, it is associated with an increased adipocyte thermogenic program characterized by activation of the ATF2 pathway, which correlates with higher UCP1 and FGF21 levels. Consequently, mice lacking the upstream activators of p38 kinases in T cells were protected against diet-induced obesity (DIO) and AT inflammation, along with an improved metabolic profile characterized by enhanced browning and reduced liver steatosis. Our findings highlight the role of p38 signaling in reducing Treg accumulation in AT and identifies this kinase family as an important regulator in T cell function during obesity. In addition, we identify IL-35 as a potential therapeutic target for immunotherapy aimed at combating obesity.

Results

Lack of MKK3/6 in T cells protects against HFD-induced obesity, type 2 diabetes, and liver steatosis

The significance of the p38 kinase family in innate cells, such as macrophages and neutrophils, in relation to obesity and metabolic diseases, has been extensively researched (Nikolic et al, 2020). However, the role of this stress kinase family in T cells during obesity is not fully understood. As an initial step, we took advantage of the data available from single-cell RNA sequencing of human AT from White Adipose Atlas (Emont et al, 2022) and examined the expression pattern of the p38 signaling pathway in the cluster of T cells infiltrating AT from lean individuals (BMI < 30) and patients with obesity (BMI 30–40) or severe obesity (BMI 40–50) (Fig. 1A and Dataset EV1). Patients with severe obesity (BMI 40–50) exhibited a signature of activation of p38 pathway in T cells from AT, as opposed to lean individuals (BMI 20–30). Precisely, we found higher expression of p38α (*MAPK14*), its upstream activator, MKK6 (*MAP2K6*), and its substrate *ATF2*, along with down-expression of the negative regulator the phosphatase *DUSP1* (Fig. 1B,C). All together, these data suggest that the p38 signaling pathway has a role in T cells during obesity.

To evaluate this hypothesis, we generated mice lacking the p38 upstream activators, MKK3 and MKK6, specifically in conventional T cells (MKK3/6$^{CD4\text{-}KO}$). Both kinases were specifically deleted in CD4$^+$ and CD8$^+$ T cells, whereas expression was unaffected in other cell types and tissues (NK, liver, and AT) (Appendix Fig. S1A). Since previous studies using mice lacking p38 family members (Hayakawa et al, 2017; Risco et al, 2018) showed lymphoid dystrophy, we evaluated whether the lack of p38 activation results in lymphocyte abnormalities. Analysis of thymus, spleen and peripheral lymphoid organs' weight and cell number showed no differences in MKK3/6$^{CD4\text{-}KO}$ mice compared to control mice CD4-Cre (Appendix Fig. S1B,C). In addition, we did not observe differences in T cell development in the thymus (Appendix Fig. S1D). Furthermore, we measured real-time bioenergetic changes in naive CD4$^+$ T cells activated with PMA/Ionomycin and found no differences between genotypes (Appendix Fig. S1E). These data suggest that, unlike p38 deficiency, the lack of p38 activation in T cells does not induce lymphoid dystrophy or problems in T cell activation.

Interestingly, MKK3/6$^{CD4\text{-}KO}$ mice were leaner than control CD4-Cre mice and showed lower epididymal WAT (eWAT) and subcutaneous WAT (sWAT) weight (Appendix Fig. S1F,G). Metabolic cages analysis suggested a trend towards increased energy expenditure (EE) in chow-diet-fed MKK3/6$^{CD4\text{-}KO}$ mice (Fig. EV1A), without differences in food intake or locomotor activity (Fig. EV1B). In addition, chow-diet-fed MKK3/6$^{CD4\text{-}KO}$ mice presented elevated brown adipose tissue (BAT) thermogenesis, determined by higher interscapular temperature (Fig. EV1C,D), compared to both CD4-Cre mice and their littermates (MKK3/6$^{f/f}$). These data suggest that p38 activation in T cells regulates BAT temperature and energy homeostasis. In addition, it might have an important role in the development of obesity-associated metabolic diseases.

To further elucidate the contribution of p38 activation in T cells during obesity, we fed animals a high-fat diet (HFD) for 8 weeks. MKK3/6$^{CD4\text{-}KO}$ mice were protected from HFD-induced obesity compared to CD4-Cre mice (Fig. 2A). The lower body weight was correlated with reduced body and fat mass, as measured by MRI (Fig. 2B), reduced fat-depot and liver mass (Fig. 2C), without differences in food intake (Fig. 2D). A similar phenotype was observed in MKK3/6$^{CD4\text{-}KO}$ female mice (Figs. EV2A–C). While metabolic cages analysis from these animals did not show differences in EE (Kcal/h) (Fig. 2E,F), when EE corrected by lean mass was performed, we observed an increase of EE in HFD-fed MKK3/6$^{CD4\text{-}KO}$ mice compared to those in CD4-Cre control mice (Fig. 2G,H). Since obesity is usually followed by hyperglycemia and ectopic fat accumulation in liver (also known as liver steatosis) (Nikolic et al, 2020), analysis of blood glucose and liver histology showed protection against hyperglycemia and steatosis in HFD-fed MKK3/6$^{CD4\text{-}KO}$ mice (Fig. 2I,J). We also performed glucose and insulin tolerance test (GTT and ITT), and found no differences in glucose tolerance but significantly improved insulin sensitivity in HFD-fed MKK3/6$^{CD4\text{-}KO}$ mice (Appendix Fig. S2A,B).

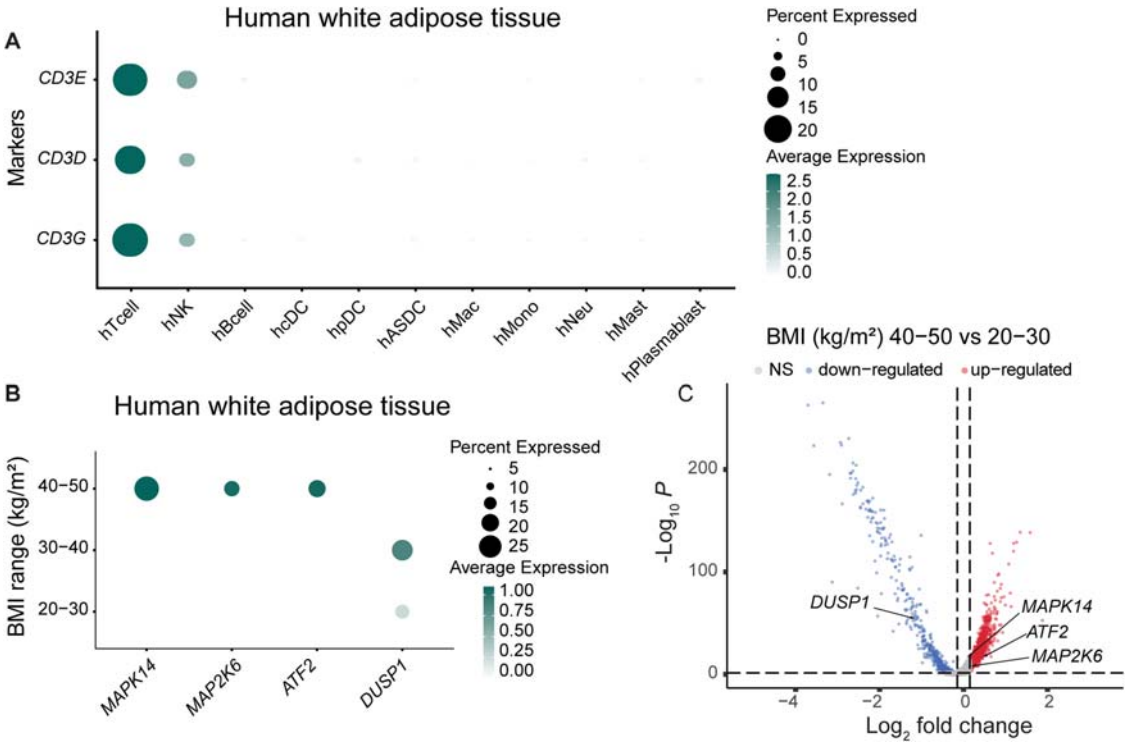

Figure 1. p38 MAPK pathway is upregulated in T cells in obese human white adipose tissue.

(**A**) Dot plot illustrating the expression of the indicated T cell marker genes in the different cell type clusters in human white AT single-cell RNA-seq data from Emont et al (2022). (**B**) Dot plot showing the expression of the indicated genes by BMI range in human white AT T cell cluster shown in (**A**). (**C**) Volcano plot of differentially expressed genes in human white AT T cell cluster in severe obese (BMI 40–50 kg/m^2) versus non-obese (BMI 20–30 kg/m^2) subjects. The vertical dashed line indicates a log2 fold change cut-off of 0.15. The horizontal dashed line indicates a −log10 adjusted *p*-value (using Bonferroni correction) cut-off of 1.3 (adj *p*-value < 0.05). Data information: Differentially expressed genes between BMI ranges were identified with a non-parametric Wilcoxon rank sum test. Obese (BMI 40–50 kg/m^2) $n = 6$ biologically independent patients; Non-obese (BMI 20–30 kg/m^2) $n = 10$ biologically independent patients; DC: dendritic cells; Mac: macrophages; Mono: monocytes; Neu: neutrophils; Mast: mastocytes. Source data are available online for this figure.

In addition, we observed protection against DIO in MKK3/6$^{CD4\text{-}KO}$ mice compared with their MKK3/6$^{f/f}$ littermates (Fig. 3A,B). The results from metabolic cages indicated that DIO was not due to impaired intestinal absorption of lipids or to higher locomotor activity, as HFD-fed MKK3/6$^{CD4\text{-}KO}$ mice actually showed higher lipid absorption and reduced locomotor activity (Fig. 3C,D). Interestingly, HFD-fed MKK3/6$^{CD4\text{-}KO}$ mice exhibited higher BAT temperature compared to littermates (Fig. 3E). Moreover, we observed that the protection against obesity and the increase in BAT temperature also occur in HFD-fed MKK3/6$^{CD4\text{-}KO}$ female mice (Fig. EV2D).

Deficiency of MKK3/6 in T cells increases adipose tissue thermogenesis and browning

Our group has shown that the immune system regulates body weight by influencing AT thermogenesis (Crespo et al, 2023), and we observed higher BAT temperature in mice lacking p38 activation in T cells. To confirm these differences under thermoneutral conditions, we placed CD4-Cre and MKK3/6$^{CD4\text{-}KO}$ mice at 30 °C throughout the entire HFD feeding. We observed that under isothermal housing, MKK3/6$^{CD4\text{-}KO}$ mice maintained their protection against HFD-induced obesity (Fig. 4A) showing reduced body and fat mass evaluated by MRI (Fig. 4B), reduced fat depots (Fig. 4C), adiposity (Fig. 4D) and liver steatosis (Fig. 4D). In addition, MKK3/6$^{CD4\text{-}KO}$ mice preserved higher BAT temperature at thermoneutrality (Fig. 4E), confirming that protection against obesity is autonomous and independent of animal housing temperature. In addition, we injected mice with norepinephrine (NE, 1 mg/kg of BW) to evaluate thermogenic capacity of mice at thermoneutrality. Our results showed that HFD-fed MKK3/6$^{CD4\text{-}KO}$ mice maintained higher basal BAT temperature after 4 weeks at thermoneutrality; when stimulated with NE, they reached the same peak BAT temperature peak as control MKK3/6$^{f/f}$ mice (Appendix Fig. S3A,B). Moreover, we analyzed the expression of thermogenic genes in BAT at thermoneutrality and we did not find a significant increase in their expression in MKK3/6$^{CD4\text{-}KO}$ mice compared to the control group, although there is a tendency for increased PGC1α expression (Appendix Fig. S3C).

Given that MKK3/6$^{CD4\text{-}KO}$ mice showed heightened BAT temperature in comparison to both littermates (Fig. 3E) and CD4-Cre (Fig. 5A), we conducted a histological analysis of BAT morphology. The histological analysis unveiled increased cellularity and maintained BAT morphology in MKK3/6$^{CD4\text{-}KO}$ mice, characterized by typical multilocular lipid droplets (Fig. 5B). Multilocular cells with high energy-dispensing activity have been linked to elevated expression of the mitochondrial BAT marker UCP1 (Leiva et al, 2020). UCP1 is a crucial mitochondrial protein

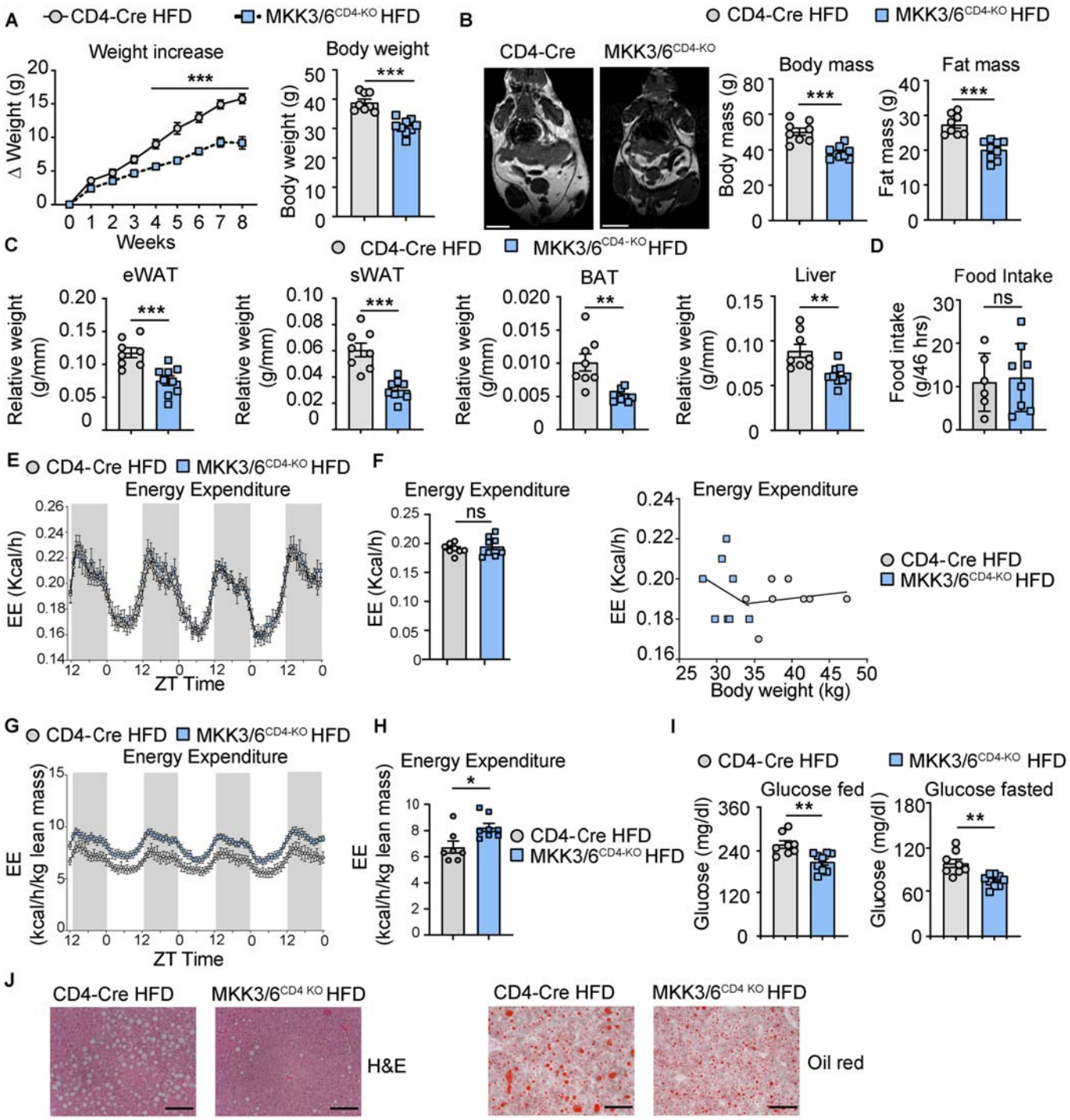

involved in BAT thermogenesis, which uncouples oxidative phosphorylation from ATP production, therefore dissipating chemical energy as heat (Enerbäck et al, 1997). Quantitative RT-PCR and western blot analysis confirmed high UCP1 expression in BAT from HFD-fed MKK3/6$^{CD4\text{-}KO}$ mice (Fig. 5C,D), correlating with BAT activation and elevated thermogenesis-related genes, *Fgf21* and its target *Ppargc1a* in HFD-fed MKK3/6$^{CD4\text{-}KO}$ mice (Fig. 5D). It has been shown that FGF21 acts as an autocrine factor in adipocytes, inducing UCP1 expression and promoting the thermogenic program (Reilly et al, 2021). These results may indicate that deficiency of p38 activation in T cells promotes BAT thermogenesis thus restraining obesity development.

T cells have been shown to regulate the browning of WAT (Kohlgruber et al, 2018; Moysidou et al, 2018), as well as adipose-derived FGF21 in an autocrine/paracrine manner (Fisher et al, 2012). Therefore, we evaluated whether the lack of p38 activation in T cells induced browning. We found significant upregulation of the browning-signature markers *Ucp1*, PR domain-containing16

Figure 2. MKK3/6 deficiency in T cells protects against HFD-induced obesity.

(**A–J**) MKK3/6$^{CD4\text{-}KO}$ and CD4-Cre mice were fed a high-fat diet (HFD) for 8 weeks (starting at 8–10 weeks old). (**A**) Body weight evolution in MKK3/6$^{CD4\text{-}KO}$ and CD4-Cre male mice for 8 weeks. Data are presented as the increase above initial weight (left) and absolute weight at the end of the experiment (right). (**B**) MRI analysis of body and fat mass in CD4-Cre and MKK3/6$^{CD4\text{-}KO}$ mice after 8 weeks of HFD. Representative images are shown on the left. (**C**) eWAT, sWAT, BAT, and liver mass relative to tibia length. (**D**) Food intake during 46 h. (**E**, **F**) Comparison of energy balance between HFD-fed MKK3/6$^{CD4\text{-}KO}$ and CD4-Cre mice examined in metabolic cages. Hour-by-hour variation in EE (kcal/h) (**E**); mean EE (Kcal/h) and ANCOVA analysis of EE (kcal/h) (**F**). (**G**, **H**) Comparison of energy balance between HFD-fed MKK3/6$^{CD4\text{-}KO}$ and CD4-Cre mice examined in metabolic cages. Hour-by-hour lean-mass-corrected variation in EE (kcal/h/kg) (**G**) and mean lean mass-corrected EE (kcal/h/kg) (**H**). (**I**) Blood glucose concentration after 8 weeks of HFD in mice fed (left) or fasted overnight (right). (**J**) Representative haematoxylin–eosin and oil-red O staining of liver sections. Data Information: Data are presented as mean ± SEM, $*p < 0.05$, $**p < 0.01$, $***p < 0.001$, ns: not significant. Analysis by 2-way ANOVA coupled to the Bonferroni post-test (**A**) or coupled to the Sidak's multiple comparison post-test (**E**, **G**); and by *t* test or by the Welch test when variances were different (**A–C**, **F**, **H**, **I**). $n = 6$–9 biologically independent mice for each group, represented as single dots in the graphs (**A–I**). Scale bar: 1 cm (**B**), 100 µm (**J**). Source data are available online for this figure.

(*Prdm16*), and peroxisome proliferator-activated receptor gamma (*Ppargc1*) in eWAT and sWAT from HFD-fed MKK3/6$^{CD4\text{-}KO}$ mice (Fig. 5E,G). We also observed smaller adipocyte size in both eWAT and sWAT from HFD-fed MKK3/6$^{CD4\text{-}KO}$ mice (Fig. 5F,H). Considering the association of obesity with impaired AT metabolism (Leiva et al, 2020) and the emerging evidence for the role of T lymphocytes in the regulation of AT (Mathis, 2013), we profiled metabolism-related gene expression in eWAT and sWAT from HFD-fed MKK3/6$^{CD4\text{-}KO}$. RT-PCR revealed increased expression of genes involved in adipogenesis (*AdipoQ* and *Plin1*), lipogenesis (*Ppard, Acaca*, and *Scd1*), β-oxidation (*Acox1* and *Cpt1*), and glycolysis (*Pepck*) in both eWAT and sWAT (Fig. EV3A,B). These results provide evidence for a T cell–AT crosstalk, regulated by p38 activation, that controls AT metabolism and browning, especially in obesity.

T cell MKK3/6-deficiency increases Treg accumulation and prevents CD8$^+$ infiltration into adipose tissues

Obesity is considered as low-grade inflammation condition, so we next examined the cellular mechanism underlying the observed DIO protection by flow cytometry (gating strategy presented in Appendix Fig. S4). First, we analyzed CD4$^+$, CD8$^+$ and Treg population in the spleen, blood, and AT draining lymph node after HFD. While there were no differences in CD4$^+$ and CD8$^+$ cells in the observed lymphoid compartments and circulation (Figs. EV4A–C), we found more Treg cells in the spleen, blood, and lymph nodes in mice deficient for p38 activation in T cells after HFD (Figs. EV4A–C), consistent with previously published data showing that p38 deficiency enhances Treg induction (Hayakawa et al, 2017). Obesity leads to decrease of protective Treg cells in AT (Feuerer et al, 2009), hence we analyzed if the higher frequency of Treg cells observed in MKK3/6$^{CD4\text{-}KO}$ mice was also evident in AT. Our results demonstrate that p38 activation in T cells inhibits Treg cell accumulation in AT and, as a result, HFD-fed MKK3/6$^{CD4\text{-}KO}$ mice show AT Treg cell expansion (Fig. 6A; Appendix Fig. S5). To rule out that these changes were due to a leaner phenotype, we analyzed AT Treg cell population in mice after 2 weeks of HFD where there were no differences in body or fat depots weight (Appendix Fig. S6A,B). We found an increased frequency of Treg cells in lymph nodes and circulation (Appendix Fig. S6C,D), suggesting that Treg cells were migrating to inflamed tissue, such as AT during obesity. Although we found a lower percentage of Treg cells in eWAT in MKK3/6$^{CD4\text{-}KO}$ mice, the number of cells per gram of tissue was higher compared to littermates (Appendix Fig. S6E). These data suggest that while MKK3/6$^{CD4\text{-}KO}$ mice have more Treg cells in eWAT, the number of Treg cells declines in littermates shortly after starting the HFD. To corroborate this, we checked whether p38 signaling pathway was differentially expressed in the cluster of Treg cells in the White Adipose Atlas (Emont et al, 2022) (Fig. EV5A). We observed higher expression of p38α (*MAPK14*) in AT Treg cells from human with obesity (BMI 30–50) or with severe obesity (BMI 40–50) compared with lean individuals (BMI 20–30) (Figs. EV5B–EV5E and Datasets EV2 and EV3). We also found that its upstream activators, MKK6 (*MAP2K6*, Fig. EV5B) and MKK3 (*MAP2K3*), were upregulated in Treg cells from human with obesity (Figs. EV5B,F,G and Dataset EV4). In Treg cells from humans with severe obesity, the expression of phosphatase *DUSP1* was downregulated (Fig. EV5B), while *ATF-2* was also upregulated in AT Treg cells from humans with a BMI 40–50 (Fig. EV5B). Altogether, these data indicate that p38 signaling pathway is upregulated in Treg cells from the AT of humans with obesity.

Since Treg cells possess immunosuppressive properties and may play a role in suppressing infiltration of CD8$^+$ obesogenic T cells in AT (Burzyn et al, 2013; Feuerer et al, 2009), we measured CD8$^+$ T cells in eWAT by FACS. HFD-fed MKK3/6$^{CD4\text{-}KO}$ mice exhibit lower infiltration of CD8$^+$ cells in eWAT than HFD-fed CD4-Cre mice (Fig. 6B). CD8$^+$ cell infiltration precedes macrophage accumulation and promotes pro-inflammatory macrophage recruitment (Nishimura et al, 2009). In line with this, eWAT from HFD-fed MKK3/6$^{CD4\text{-}KO}$ mice presented less abundance of obesogenic, pro-inflammatory macrophages and NK cells (Fig. 6C). Notably, we found a higher frequency of anti-inflammatory macrophages (F4/80$^+$CD11b$^+$CD206$^+$) after 2 weeks of HFD, a condition that is maintained after 10 weeks of HFD (Appendix Fig. S6E). These data suggest that p38 activation deficiency in T cells prevents AT inflammation.

p38 activation in Treg cells represses the expression of *Il-35* via the mTOR pathway

To investigate the molecular mechanisms through which Treg cells control AT inflammation, we assessed the expression of IL-35, an immunosuppressive cytokine produced by Treg cells, in both the AT and stromal vascular fraction (SVF). The expression of *Ebi3* and *p35*, the two subunits of the IL-35, were upregulated in HFD-fed MKK3/6$^{CD4\text{-}KO}$ SVF (Fig. 7A,B), highlighting p38s as regulators of IL-35 production in Treg cells. To confirm this, we analyzed

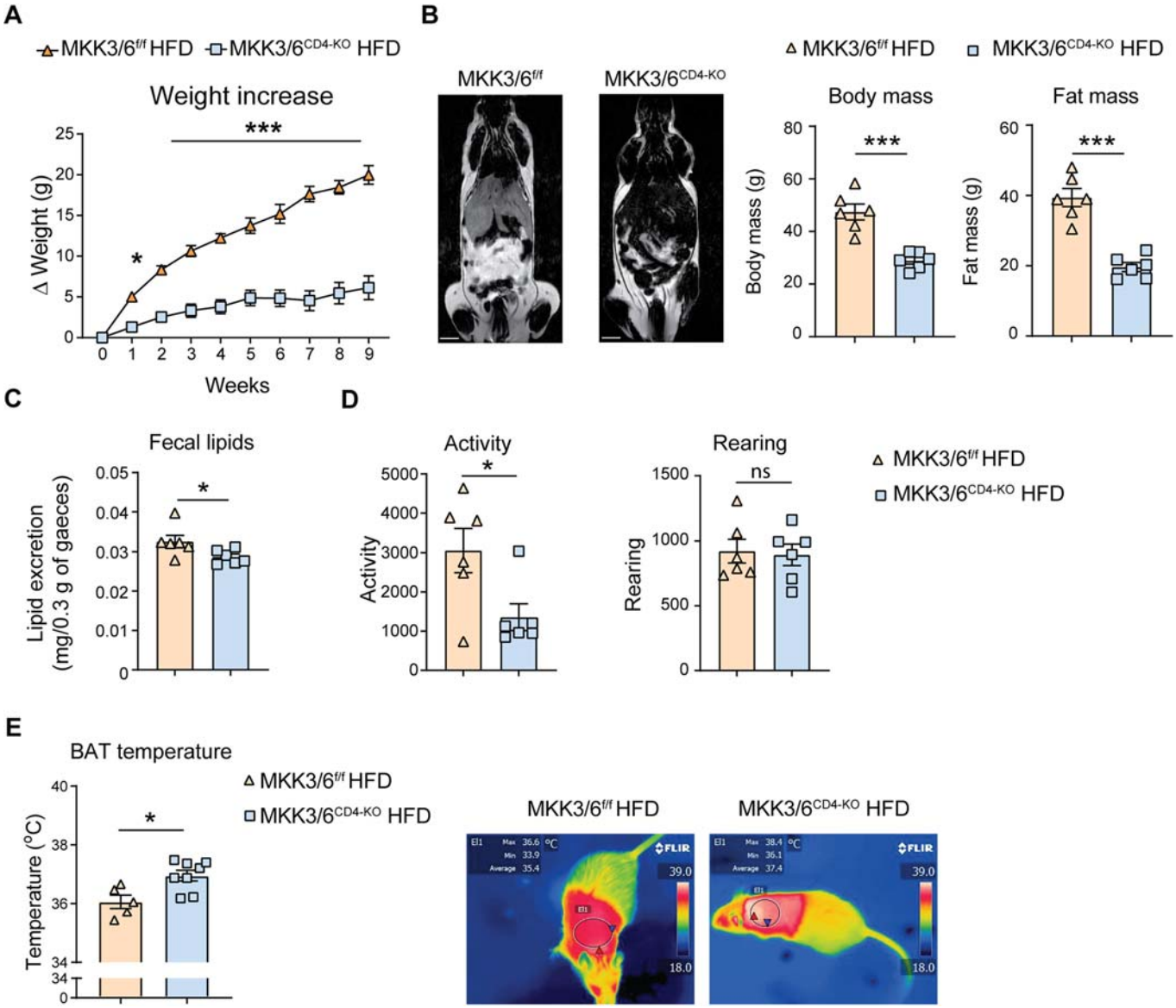

Figure 3. MKK3/6 deficiency in T cells protects against HFD-induced obesity by increasing BAT temperature.

(A–E) MKK3/6$^{CD4\text{-}KO}$ and MKK3/6$^{f/f}$ mice were fed a high-fat diet (HFD) for 9 weeks. **(A)** Body weight increased for 9 weeks. **(B)** MRI analysis of body and fat mass and representative images on the left. **(C)** Fecal lipid excretion over 5 days. **(D)** Locomotor activity and rearing over 24 h. **(E)** Skin temperature surrounding interscapular BAT. Right panels show representative infrared thermal images. Data Information: Data are presented as mean ± SEM, $*p < 0.05$, $***p < 0.001$, ns: not significant. Analysis by 2-way ANOVA coupled to the Sidak's multiple comparison post-test **(A)** or *t* test or by the Welch test when variances were different **(B–E)**. $n = 6$–8 biologically independent l'mmice for each group, represented as single dots in the graphs **(A–E)**. Scale bar: 1 cm **(B)**. Source data are available online for this figure.

IL-35^{+} Treg cells in AT draining lymph nodes after HFD, and we observed a higher frequency of IL-35^{+} Treg cells in HFD-fed MKK3/6$^{CD4\text{-}KO}$ mice (Fig. 7C). To gain deeper insights into the molecular mechanism underlying the control of IL-35 production by p38 activation, we next measured *Il-35* expression in in Hvitro induced Treg cells (iTregs) (Fig. 7D). Consistent with the in vivo data from SVF and lymph nodes, the expression of *Il-35* (p35) was higher in MKK3/6$^{CD4\text{-}KO}$ Treg cells than in their CD4-Cre counterparts (Fig. 7D). To confirm the action of this pathway in human Treg cells, we inhibited p38 with the p38 pan inhibitor BIRB796 (Kuma et al, 2005). As expected, p38 inhibition in human Treg cells induced the expression of *Il-35* (*P35*) (Fig. 7E).

Previous studies have proposed a potential role of mTOR in regulating IL-35 levels (Zhang et al, 2017). In agreement, we found that Treg cells from mice with increased mTOR activation (TSC1$^{CD4\text{-}KO}$ mice) presented higher levels of IL-35 (Fig. 7F). mTOR has been shown to be modulated by p38 (Gonzalez-Teran et al, 2016a). In agreement, western blot analysis demonstrated that the lack of p38 activation in Treg cells leads to increased mTOR activation and higher S6 protein phosphorylation (Fig. 7G).

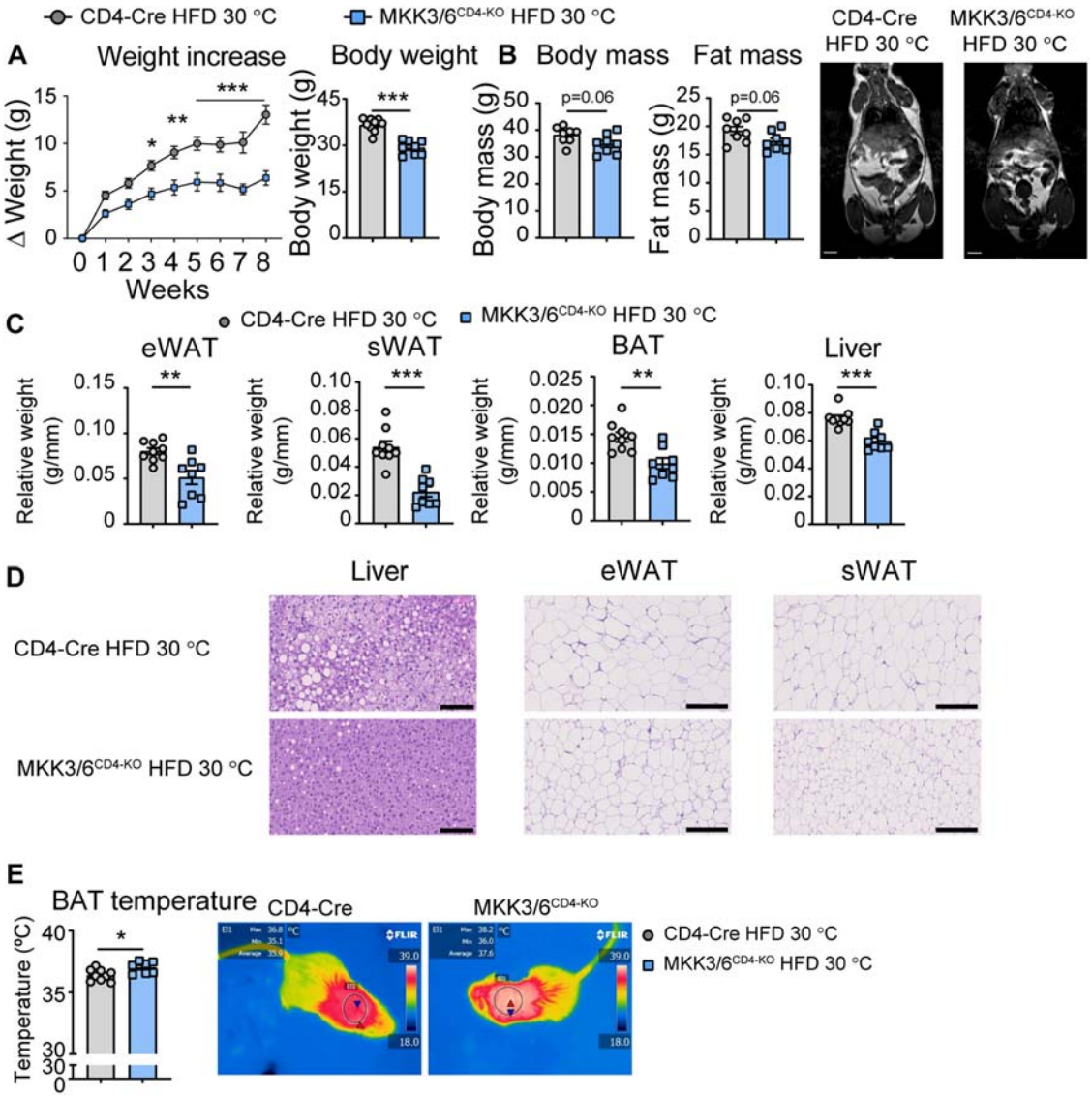

Figure 4. MKK3/6 deficiency in T cells protects against HFD-induced obesity in isothermal housing.

(**A–E**) MKK3/6$^{CD4\text{-}KO}$ and CD4-Cre mice were fed a high-fat diet (HFD) for 8 weeks (starting at 8–10 weeks old) and housed at 30 °C during whole course of HFD. (**A**) Body weight evolution in CD4-Cre and MKK3/6$^{CD4\text{-}KO}$ male mice for 8 weeks. Data are presented as the increase above initial weight (left) and absolute weight at the end of the experiment (right). (**B**) MRI analysis of body and fat mass in MKK3/6$^{CD4\text{-}KO}$ and CD4-Cre mice after 8 weeks of HFD. Representative images are shown on the right. (**C**) eWAT, sWAT, BAT, and liver mass relative to tibia length. (**D**) Representative haematoxylin–eosin and oil-red O staining of liver, eWAT, and sWAT sections. (**E**) Skin temperature surrounding interscapular BAT. Right panels show representative infrared thermal images. Data information: Data are presented as mean ± SEM, $*p < 0.05$, $**p < 0.01$, $***p < 0.001$. Exact p-values are shown. Analysis by 2-way ANOVA coupled to the Bonferroni post-test (**B**) or *t* test or by the Welch test when variances were different (**A–C**, **E**). $n = 7$–9 biologically independent mice for each group, represented as single dots in the graphs. Scale bar: 1 cm (**B**), 100 µm for liver and 250 µm for eWAT and sWAT (**D**). Source data are available online for this figure.

To evaluate whether mTOR activation in MKK3/6$^{CD4\text{-}KO}$ Treg cells was responsible for the increase in IL35 expression, we inhibited mTOR pathway with rapamycin. We found that IL-35 expression is dependent on mTOR activation, since treating Treg cells lacking p38 activation (MKK3/6$^{CD4\text{-}KO}$) with rapamycin diminished the IL-35 expression (Fig. 7H). In summary, we described novel mechanism by which p38 kinases inhibits the mTOR signaling pathway that, in turn, reduces IL-35 production in mouse and human Treg cells. Inhibiting of p38s, either genetically or chemically, increased IL-35 mRNA and protein levels.

Treg-derived IL-35 triggers adipose tissue browning and is reduced in obese patients

As MKK3/6$^{CD4\text{-}KO}$ mice expressed higher levels of IL-35 in AT, we postulated that IL-35 might have a role in AT thermogenesis and, consequently, in protection against obesity. Interestingly, we found a tendency for lower p35 expression in visceral AT obtained from individuals with obesity compared to lean individuals (Fig. 8A). In addition, MKK3/6$^{CD4\text{-}KO}$ mice exposed to cold preserved their body and BAT temperature, while the temperature of control CD4-Cre

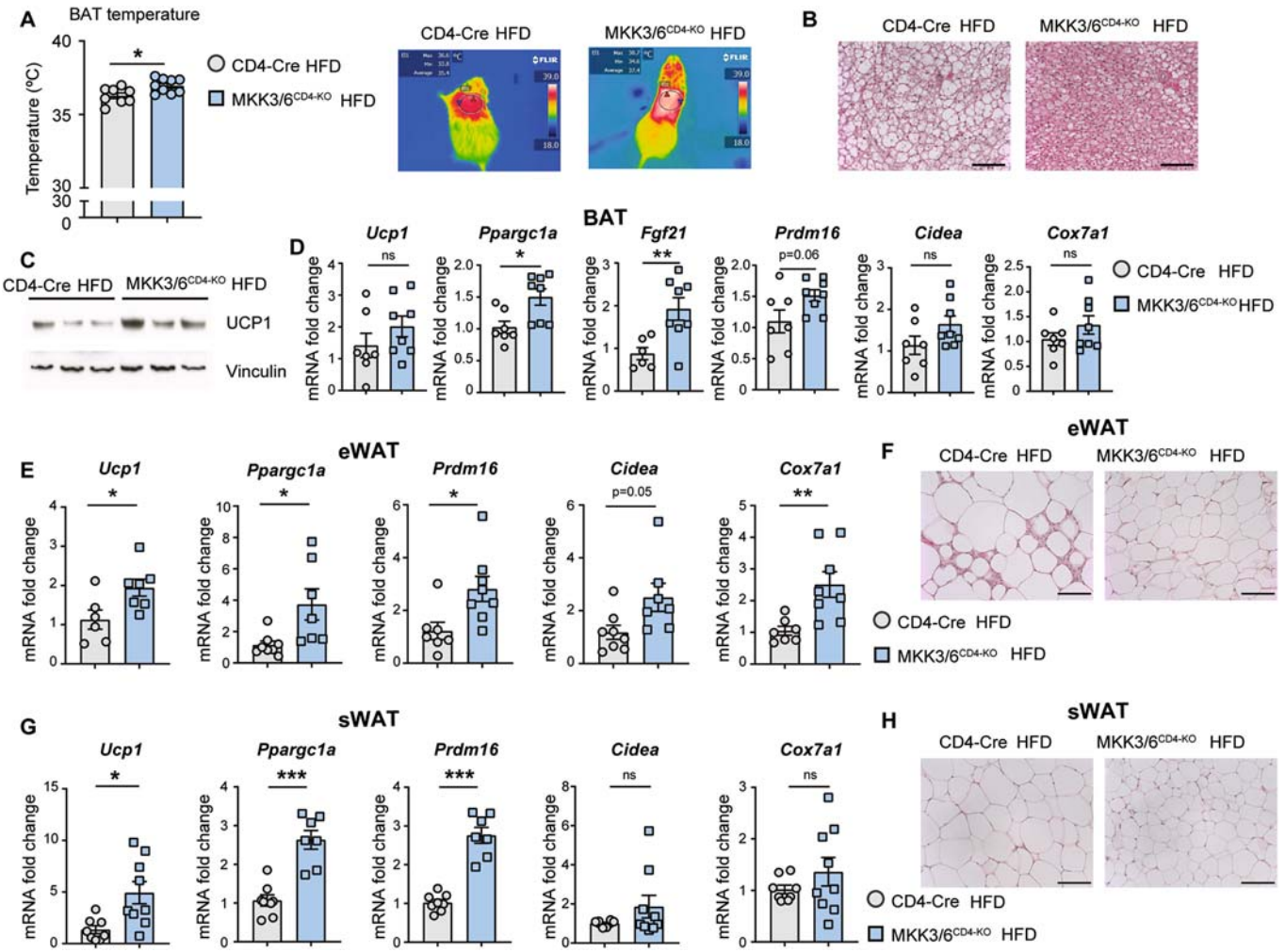

Figure 5. Lack of MKK3/6 in T cells increases BAT thermogenesis and adipose tissue browning.

(**A–H**) MKK3/6$^{CD4\text{-}KO}$ and control CD4-Cre mice were HFD-fed for 8 weeks. (**A**) Skin temperature surrounding interscapular BAT. Right panels show representative infrared thermal images. (**B**) Representative H&E staining of BAT sections. (**C**) Western blot analysis of UCP1 in BAT. (**D**) qRT-PCR analysis of thermogenic gene mRNA expression in BAT isolated from control or MKK3/6$^{CD4\text{-}KO}$ mice. mRNA expression was normalized to the expression of β-actin mRNA and presented as fold increase compared to CD4-Cre. (**E**) qRT-PCR analysis of browning genes mRNA expression from eWAT isolated from control or MKK3/6$^{CD4\text{-}KO}$ mice. mRNA expression was normalized to β-actin mRNA and presented as fold increase compared to CD4-Cre. (**F**) Representative H&E staining of eWAT sections. (**G**) qRT-PCR analysis of browning genes mRNA expression from sWAT isolated from control or MKK3/6$^{CD4\text{-}KO}$ mice. mRNA expression was normalized to β-actin mRNA and presented as fold increase compared to CD4-Cre. (**H**) Representative H&E staining of sWAT sections. Data information: Data are presented as mean ± SEM, $*p < 0.05$, $**p < 0.01$, $***p < 0.001$, ns: not significant. Exact *p*-values are shown. Analysis by t test or by the Welch test when variances were different. $n = 7$–9 biologically independent mice for each group, represented as single dots in the graphs. Scale bar: 100 μm (**B**, **F**, **H**). Source data are available online for this figure.

mice gradually dropped during cold challenge (Fig. 8B). We next evaluated the functional role of IL-35 in thermogenesis in vivo. IL-35 injection triggered thermogenesis in mice compared to the PBS-treated group (Fig. 8C). To understand mechanistically how IL-35 cytokine controls thermogenesis in adipocytes, we treated brown adipocytes with IL-35 and found increased levels of UCP1 and FGF21, suggesting an activation of the brown thermogenic program (Fig. 8D). IL-35 treatment also resulted in ATF-2 phosphorylation (Fig. 8E), the transcription factor that controls UCP1 and PGC1A expression in BAT (Cao et al, 2004). This increase in *Ucp1* expression, induced by IL-35, was downregulated when ATF2 activation in adipocytes was blunted by using inhibitor of upstream activator of ATF2 (SB203580, p38α/β inhibitor) (Fig. 8F). Furthermore, IL-35 also promoted adipogenesis in differentiated primary adipocytes, which was reduced when ATF2 activation was suppressed (Fig. 8G). In summary, we identified possible novel role of Treg-derived cytokine IL-35 in regulating AT thermogenesis through the pATF-2/UCP1/FGF21 axis.

Discussion

Our data highlight a new role of p38 pathway in Treg cells that impairs BAT activation and browning during obesity. Our findings suggest that the molecular mechanism by which p38 activation regulates the production of IL-35 by Tregs is through the mTOR

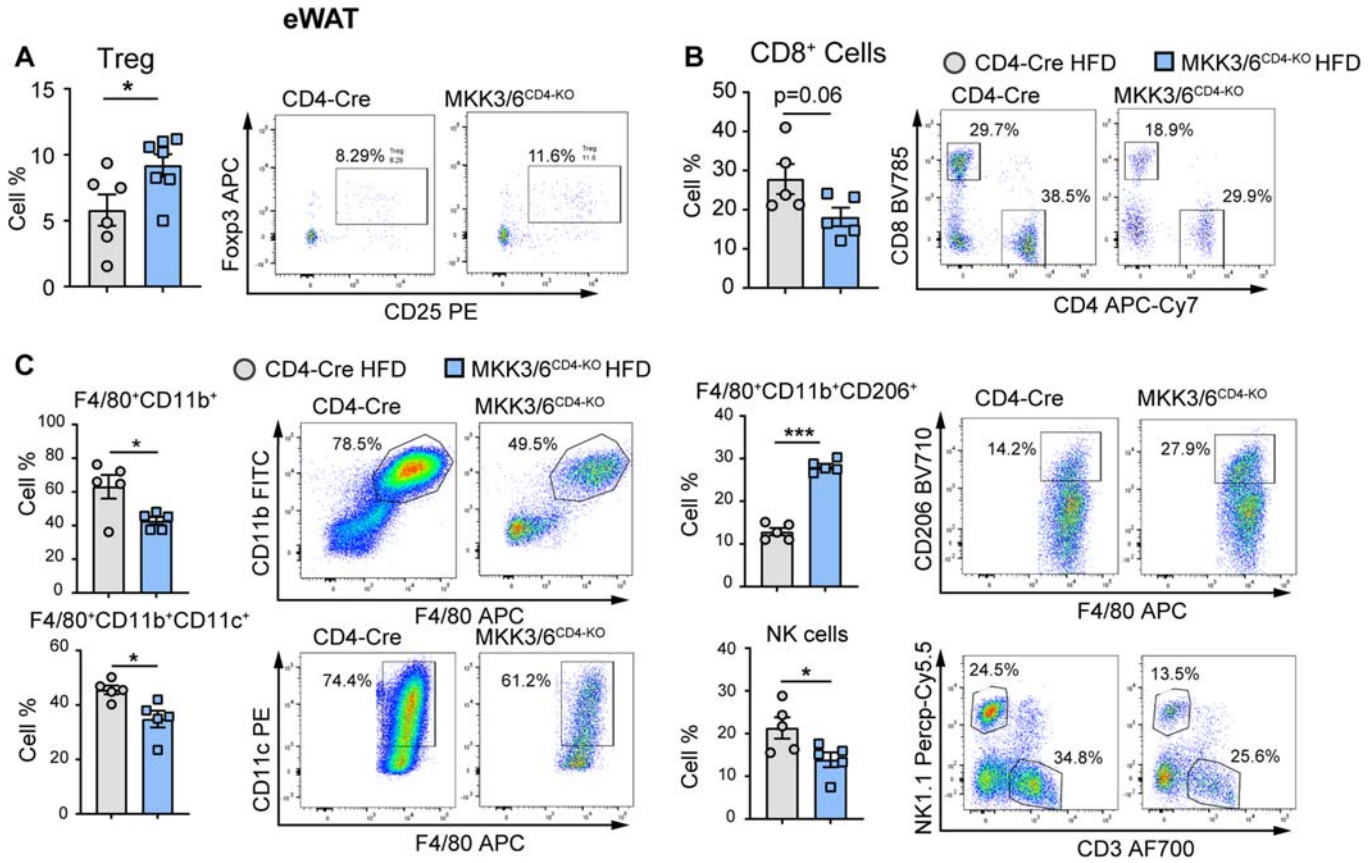

Figure 6. MKK3/6 deficiency in T cells promotes Treg cell accumulation in adipose tissue.

(**A–C**) MKK3/6$^{CD4\text{-}KO}$ and CD4-Cre mice were fed a high-fat diet (HFD) for 8 weeks. (**A**) FACS quantification and representative dot plots of Treg cells ($CD4^+CD25^+Foxp3^+$) in SVF and (**B**) $CD8^+$ T cells in SVF. (**C**) FACS quantification and representative dot plots of myeloid ($F4/80^+CD11b^+$), M1 macrophages (Mϕ) ($F4/80^+CD11b^+CD11c^+$), M2 Mϕ ($F4/80^+CD11b^+CD206^+$), and NK ($NK1.1^+CD3^-$) cells in SVF. Data Information: Data are presented as mean ± SEM, $*p < 0.05$, $***p < 0.001$. Exact *p*-values are shown. Analysis by *t* test or by the Welch test when variances were different. $n = 5$–7 biologically independent mice for each group, represented as single dots in the graphs (**A–C**). Source data are available online for this figure.

protein pathway. Furthermore, our findings suggest a potential novel role of IL35 in influencing BAT temperature. We have demonstrated that IL-35 treatment not only activates ATF-2 but also leads to increased expression of UCP1 and FGF21, coinciding with elevated BAT temperature in mice. In line with this, individuals with obesity exhibit lower expression of this cytokine in visceral fat. In summary, our findings suggest a possible role of IL-35 derived from Treg cells in controlling AT metabolism and function.

The activation of stress kinases is associated with obesity and metabolic diseases in mouse and human in a tissue-specific manner (Nikolic et al, 2020). The importance of these kinases in myeloid cells in obesity and associated comorbidities has been widely studied. For example, p38 kinases activation polarizes macrophages towards a pro-inflammatory phenotype, leading to pro-inflammatory cytokine production in a model of liver steatosis (Zhang et al, 2019) and LPS-induced acute hepatitis (Gonzalez-Teran et al, 2013). In neutrophils, p38 kinase family members control their migration and promote nonalcoholic fatty liver diseases development (Gonzalez-Teran et al, 2016b). However, our knowledge about the role of p38 kinases in T cells and their contribution to obesity development was insufficient. By analyzing the single-cell RNA sequencing data from human WAT was obtained from Emont et al (Emont et al, 2022), we focused on the expression of p38 signaling pathway in T cells and Treg cells within AT. We observed upregulated expression of p38α (*MAPK14*), its activators MKK3 (*MAP2K3*), and p38 substrate *ATF-2* in humans with obesity (BMI > 30), while *DUSP1* phosphatase, which deactivates p38s, was downregulated, suggesting a possible obesogenic role of p38 signaling pathway in both T cells and Treg cells. Furthermore, our study results confirmed p38 activation in T cells promotes obesity, as the deficiency of the upstream activators of p38 kinases, specifically in T cells, impeded obesity development and improved metabolic profiles. Our data also indicate that p38 blockade in T cells is sufficient to blunt obesity-induced AT inflammation, thereby protecting HFD-fed MKK3/6$^{CD4\text{-}KO}$ mice against the AT metabolic dysfunction known to be a driver of obesity comorbidities. Treg cells increase in lean individuals and are thought to prevent AT inflammation. Interestingly, we found a higher number of Treg cells in the blood, lymph nodes and AT of HFD-fed MKK3/6$^{CD4\text{-}KO}$ mice, resembling the phenotype typical for lean mice (Feuerer et al, 2009).

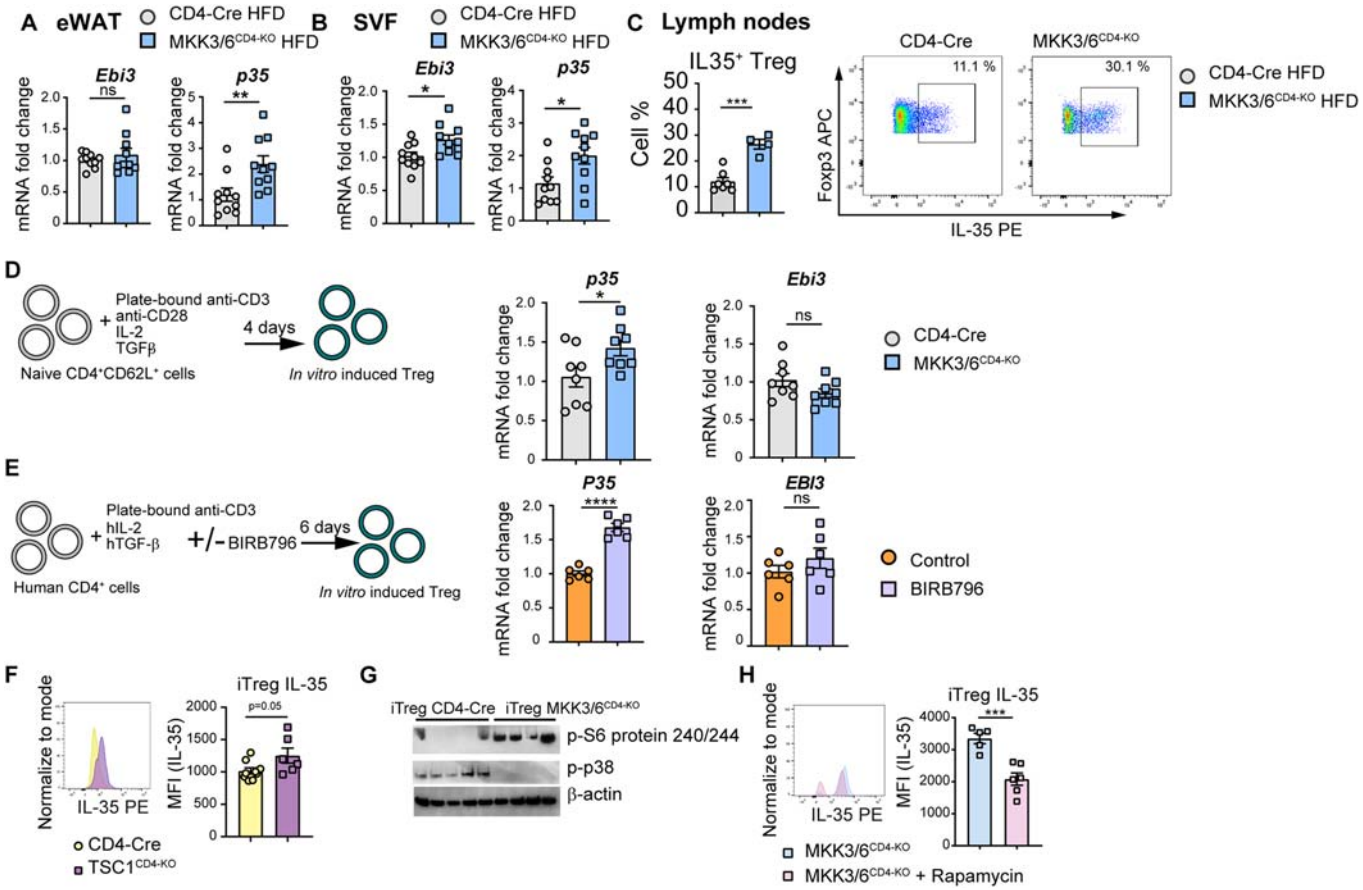

Figure 7. p38 activation in Treg cells inhibits IL-35 production.

(A–C) MKK3/6$^{CD4\text{-}KO}$ and CD4-Cre mice were fed a high-fat diet (HFD) for 8 weeks. **(A, B)** qRT-PCR analysis of mRNA expression in **(A)** eWAT and **(B)** SVF isolated from control or MKK3/6$^{CD4\text{-}KO}$ mice. mRNA expression was normalized to *b-actin* mRNA. **(C)** FACS quantification and representative dot plots of IL-35^{+} Treg cells in lymph nodes. **(D)** In vitro Treg cell induction (iTreg). Naive CD4^{+} T cells were isolated from the spleens of CD4-Cre and MKK3/6$^{CD4\text{-}KO}$ mice stimulated for 96 h with plate-bound anti-CD3, soluble anti-CD28 + IL-2 + TGFβ. qRT-PCR analysis of *p35* and *Ebi3* mRNA in iTregs derived from control or MKK3/6$^{CD4\text{-}KO}$ mice. mRNA expression was normalized to *b-actin* mRNA. **(E)** Induction of iTregs from CD4^{+} T cells isolated from healthy human donor buffy coats and stimulated with plate-bound anti-CD3, soluble hIL-2 + hTGFβ for 6 days in the presence or absence of the p38 pan inhibitor BIRB796. qRT-PCR analysis of *P35* and *EBI3* mRNA in iTregs. mRNA expression was normalized to *GAPDH* mRNA. **(F)** FACS analysis of IL-35 MFI in in vitro induced iTreg cells from CD4-Cre and TSC1$^{CD4\text{-}KO}$ mice. **(G)** Western blot analysis of p-s6 protein S240/244 and p-p38 Thr180/Tyr182 in iTreg cells from CD4-Cre and MKK3/6$^{CD4\text{-}KO}$ mice. Loading control for p-p38 was run on different gel and not presented. **(H)** FACS analysis of IL-35 MFI in in vitro induced iTreg cells from MKK3/6$^{CD4\text{-}KO}$ mice in the presence or absence of rapamycin for 4 h. Data Information: Data are presented as mean ± SEM, $*p < 0.05$, $**p < 0.01$, $***p < 0.001$, ns: not significant. Exact p-values are shown. Analysis by *t* test. $n = 4$–10 biologically independent mice **(A–C)** or $n = 4$–9 biologically independent wells **(D–H)** for each group, represented as single dots in the graphs. Source data are available online for this figure.

Treg cells are important immunosuppressive cells which maintenance self-tolerance, immune homeostasis and limit chronic inflammation (Sakaguchi et al, 2010; Takeuchi and Nishikawa, 2016; Wing and Sakaguchi, 2010). The observed accumulation of Treg cells in HFD-fed MKK3/6$^{CD4\text{-}KO}$ mice restrained CD8^{+} T cell infiltration in AT, consequently limiting AT inflammation. Namely, the infiltration of CD8^{+} T cells in AT is one of the crucial steps in obesity development which precedes the activation and influx of pro-inflammatory macrophages (Nishimura et al, 2009). In agreement, we observed lower accumulation of CD8^{+} T cells in mice lacking p38 activation, which reflected in decreased infiltration of pro-inflammatory macrophages and NK cells.

Recently, cytokine IL-35 was identified as a novel inhibitory cytokine produced by Treg cells, which potentiates their suppressive activity and suppresses T cell proliferation (Collison et al, 2007). Here, we found that its expression was p38-dependent, as both chemical inhibition and genetic deficiency of p38 activation resulted in increased IL-35 expression in human and mouse Treg cells, thereby limiting AT inflammation in HFD-fed MKK3/6$^{CD4\text{-}KO}$ mice. In addition, we described a novel mechanism by which p38 kinases regulate IL-35 expression through the inhibition of the mTOR pathway.

Finally, we have demonstrated a novel role for the Treg-derived cytokine IL-35 in AT functionality. Levels of this cytokine are decreased in obese AT in both humans and mice. These results are consistent with the recently described role for another member of the same IL family, IL-27, which promotes adipocyte thermogenesis (Wang et al, 2021). Notably, the lack of p38 activation in T cells correlates with an increase in BAT temperature, protecting mice against obesity, with some limitations. One such limitation of the study is that, although we did not observe a total increase in EE in MKK3/6$^{CD4\text{-}KO}$ mice, when corrected by lean mass, MKK3/6$^{CD4\text{-}KO}$

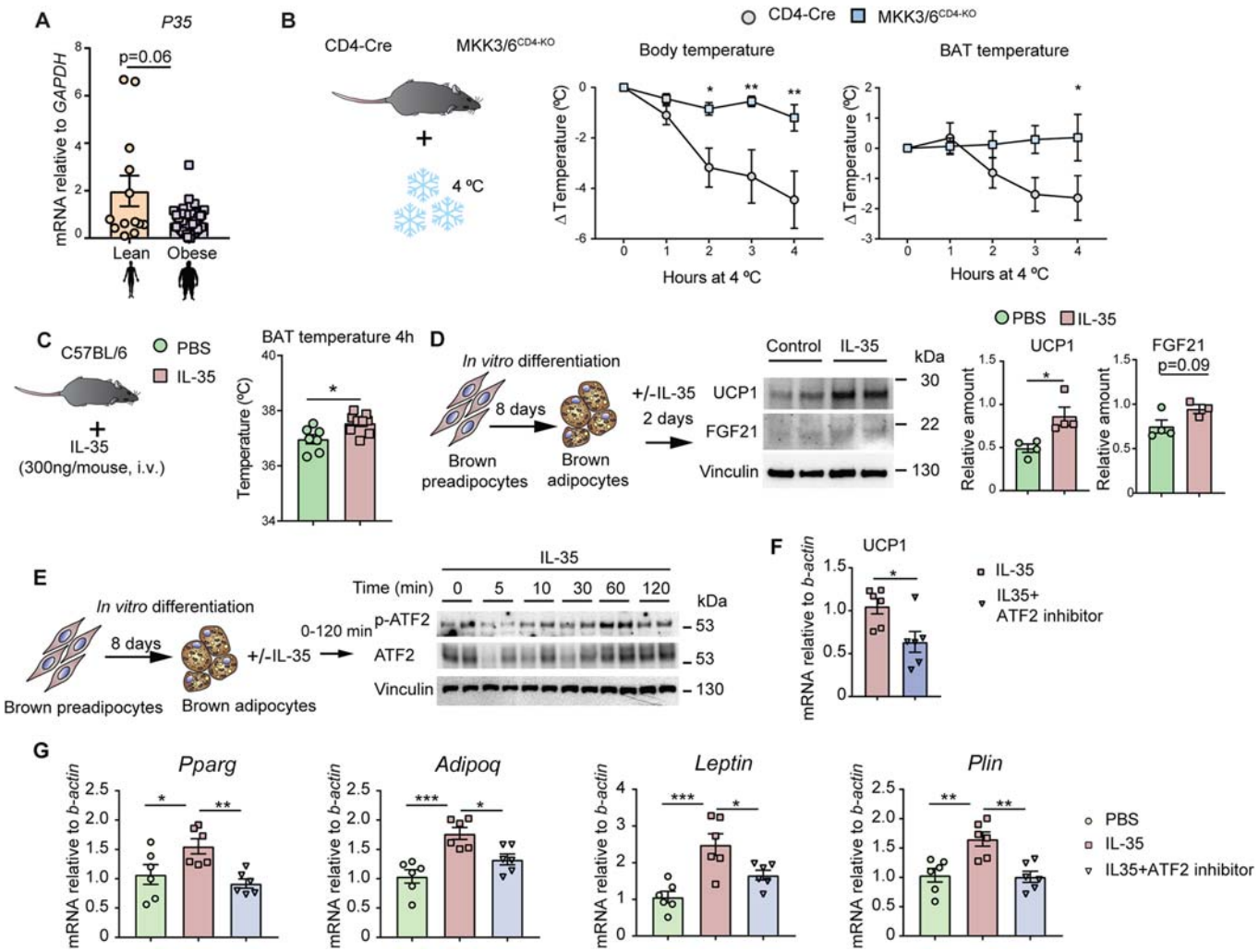

Figure 8. Treg-derived IL-35 promotes thermogenesis by increasing ATF-2 phosphorylation and UCP1 and FGF21 levels.

(A) mRNA expression of p35 subunit of IL-35 in human visceral fat isolated from lean and obese patients. **(B)** MKK3/6$^{CD4\text{-}KO}$ and control CD4-Cre mice were exposed to cold for 4 h. Body and BAT temperature was measured every hour. **(C)** C57BL6 mice were treated with recombinant IL-35 i.v. (300 ng per mouse) and BAT temperature was measured 4 h later **(D)** Immortalized brown preadipocytes were differentiated in vitro. Once differentiated, cells were stimulated in the presence or absence of IL-35 (100 ng/ml) for 48 h and UCP1 and FGF21 levels were analyzed by immunoblot. Loading control for UCP1 was run on different gel and not presented. **(E)** Immortalized brown preadipocytes were differentiated in vitro. Once differentiated, cells were stimulated in the presence or absence of IL-35 (100 ng/ml) for 0–120 min and ATF2 phosphorylation was analyzed by immunoblot. **(F)** Differentiated adipocytes were stimulated with IL-35 (100 ng/ml) for 48 h in the presence or absence of SB203580 inhibitor (10 μM). The expression of *Ucp1* level was measured by qRT-PCR and relativized to *b-actin*. **(G)** Primary white preadipocytes were isolated from C57BL6 mice and differentiated in vitro. Once differentiated, cells were stimulated with PBS or with IL-35 (100 ng/ml) for 48 h in the presence or absence of SB203580 inhibitor (10 μM). The expression of principal adipogenic markers (*Pparg*, *Adipoq*, *Leptin, Perlinipin*) level was measured by qRT-PCR and relativized to *b-actin*. Data Information: Data are presented as mean ± SEM, $*p < 0.05$, $**p < 0.01$, $***p < 0.001$. Exact *p*-values are shown. Analysis by *t* test (**A**, **C**, **D**, **F**), 2-way ANOVA (**B**), or 1-way ANOVA (**G**). Lean $N = 12$ biologically independent patients; Obese $N = 52$ biologically independent patients (**A**). $n = 5$–9 biologically independent mice (**B**, **C**) or $n = 2$–6 biologically independent wells (**D**–**G**) for each group, represented as single dots in the graphs. Source data are available online for this figure.

showed higher EE. Typically, heavier animals exhibit higher EE, whereas MKK3/6$^{CD4\text{-}KO}$ mice, being smaller, exhibit comparable EE to control mice, indicating that they have higher EE per gram of body weight. This protection was maintained when the mice were placed under isothermal conditions, confirming that the observed phenotype is dependent on p38 T cells. Since increased BAT thermogenesis is still present under isothermal housing conditions, this suggests that the effect of Treg cells/IL-35 on BAT thermogenesis is likely mediated by alternative mechanisms, which need to be confirmed by further studies. However, it is important to note that we cannot rule out the contribution of alternative mechanisms controlled by the lack of p38 activation in T cells, independent of Treg-derived IL-35, which may also play a role in protecting against obesity.

Our results suggest that the higher expression of IL-35 in MKK3/6$^{CD4\text{-}KO}$ mice might be responsible for their improved adaptive thermogenesis. In fact, we found that IL-35 is able to induce adipocyte thermogenic program. Mechanistically, IL-35 triggers the phosphorylation of the transcription factor ATF-2, leading to increased UCP1 and FGF21 protein levels in adipocytes.

While previous studies using the loss of adipose Treg cells (Bapat et al, 2015; Cipolletta et al, 2012; Feuerer et al, 2009) or gain-of function Treg cells (Matsumoto et al, 2017), did not result in significant protection against obesity, our study showed that p38 signaling pathway is important in Treg cells and may modulate their function. This ultimately led to an upregulation of IL-35 expression, which could be a contributing factor to the significant obesity protection observed in MKK3/6$^{CD4\text{-}KO}$ mice. We believe that IL-35's effects on energy balance and thermogenesis are critical components of the observed protection against obesity in this model.

In summary, our findings unveil the importance of p38 signaling in the regulation of T cell function and identify the manipulation of this pathway is a promising therapeutic strategy for metabolic diseases. We demonstrate that p38 kinases reduce Treg cells in circulation and AT draining lymph nodes, hence leading to Treg reduction in AT and obesity development. Moreover, we show that Treg-derived IL-35 has an important role in regulating AT browning via the ATF-2/UCP1/FGF21 axis, thereby improving metabolism and proposing this cytokine as a promising target for anti-obesity immunotherapy.

Methods

Reagents and tools table

Reagent/Resource	Reference or Source	Identifier or Catalog Number
Experimental Models		
C57BL/6J background	Jackson Laboratory	Cat# 000664 RRID:IMSR_JAX:000664
Tg (Cd4-cre)1Cwi/BfluJ	Jackson Laboratory	Cat# 017336 RRID:IMSR_JAX:017336
Map2k3 f/f	N/A	
Map2k6 f/f	N/A	
Recombinant DNA		
Antibodies		
APC/Cy7 anti-mouse CD4 antibody (clone RM4-5)	BioLegend	Cat# 100525 RRID:AB_312726
Brilliant Violet 785™ anti-mouse CD8a (Clone 53-6.7)	BioLegend	Cat# 100749 RRID:AB_11218801
Brilliant Violet 510™ anti-mouse CD8a Antibody (Clone 53-6.7)	BioLegend	Cat# 100752 RRID: AB_2563057
PE anti-mouse CD25 (Clone PC61)	BioLegend	Cat# 102007 RRID:AB_312856
BV421 anti-mouse CD25 (Clone A18246A)	BioLegend	Cat# 113705
PERCP-CY5.5 anti-mouse NK1.1 (Clone PK136)	BioLegend	Cat# 108728 RRID:AB_2132705
Alexa fluor 700 anti-mouse CD3 (Clone 17A2)	BioLegend	Cat# 100216 RRID:AB_493697
Brilliant Violet 711™ anti-mouse CD206 (MMR) (Clone C068C2)	BioLegend	Cat# 141727 RRID:AB_2565822
Brilliant Violet 785™ anti-mouse/human CD11b Antibody (Clone: M1/70)	BioLegend	Cat# 101243 RRID: AB_2561373
PE Hamster Anti-Mouse CD11c (Clone HL3)	BD bioscience	Cat# 553802 RRID:AB_395061
V450 anti-mouse CD45 (Clone 30-F11)	BD bioscience	Cat# 560501 RRID:AB_1645275
FITC Rat anti-mouse CD11b (Clone M1/70)	BD bioscience	Cat# 557396 RRID:AB_396679
Alexa 647 anti-Mouse F4/80 (Clone A3-1)	BioRad	Cat# MCA497A647 RRID:AB_323931
PE anti-mouse CD115 (Clon AFS98)	eBioscience	Cat #: 12-1152-82
PE-Cy7 F4/80 Monoclonal Antibody (Clone BM8)	eBioscience	Cat# 25-4801-82 RRID: AB_469653
APC anti-mouse FOXP3 (Clone FJK-16s)	eBioscience™,ThermoFisher	Cat# 17-5773-80 RRID:AB_469456
FITC anti-mouse FOXP3 (Clone FJK-16s)	eBioscience™,ThermoFisher	Cat# 11-5773-82 RRID: AB_465243
PE IL-12 p35 Monoclonal Antibody (Clone 27537)	Invitrogen, ThermoFisher	Cat# MA5-23559 RRID: AB_2609031
Anti-mouse UCP1	Abcam	Cat# AB10983 RRID:AB_2241462
Anti-mouse FGF21	BioVendor	Cat# RD281108100
Anti-mouse ATF2	Cell Signaling Technology	Cat# 9226 S
Anti-mouse p-s6 S240/244	Cell Signaling Technology	Cat# 5364 S
Anti-mouse p-p38 T180/Y182	Cell Signaling Technology	Cat# 9211 S
Anti-mouse b-actin	Santa Cruz Technology	Cat# sc-47778
Anti-mouse Vinculin	Sigma	Cat# V9131 RRID:AB_477629
Anti-mouse MKK6	Enzo Life Sciences	Cat# ADI-KAP-MA014-E RRID:AB_11179962
Anti-mouse MKK3b	Cell Signaling Technology	Cat# 9238 RRID:AB_2140797
Polyclonal goat anti-mouse IgG (H + L) Secondary Antibody, HRP	ThermoFisher	Cat# 31430 RRID:AB_228307
Polyclonal goat anti-rabbit IgG (H + L) Secondary Antibody, HRP	ThermoFisher	Cat# 31460 RRID:AB_228341

Reagent/Resource	Reference or Source	Identifier or Catalog Number
Oligonucleotides and other sequence-based reagents		
Primers for qRT-PCR	Sigma-Aldrich	
Gene	Forward	Reverse
m_b-actin	GGCTGTATTCCCCTCCATCG	CCAGTTGGTAACAATGCCATGT
m_Ucp1	GTGAACCCGACAACTTCCGAA	TGAAACTCCGGCTGAGAAGAT
m_Ppargc1a	TATGGAGTGACATAGAGTGTGCT	CCACTTCAATCCACCCAGA
m_Cox7a1	GCTCTGGTCCGGTCTTTTAGC	GTACTGGGAGGTCATTGTCGG
m_Cidea	TGACATTCATGGGATTGCAGAC	GGCCAGTTGTGATGACTAAGAC
m_Cox7a1	GCTCTGGTCCGGTCTTTTAGC	GTACTGGGAGGTCATTGTCGG
m_Prdm16	CCACCAGCGAGGACTTCAC	GGAGGACTCTCGTAGCTCGAA
m_Leptin	GAGACCCCTGTGTCGGTTC	CTGCGTGTGTGAAATGTCATT
m_Plin1	ACAGCAGAATATGCCGCCAA	GGCTGACTCCTTGTCTGGTG
m_Pepck	CCATCACCTCCTGGAAGAACA	ACCCTCAATGGGTACTCCTTC
m_G6pc	CGACTCGCTATCTCCAAGTGA	GTTGAACCAGTCTCCGACCA
m_Acox1	CCGCCACCTTCAATCCAGAG	CAAGTTCTCGATTTCTCGACG
m_Ppardelta	CTCGTACTTGAGCTTCATGCG	GAGCACACCCTTCCTTCCAG
m_Fasn	GCGGGTTCGTGAAACTGATAA	GCAAAATGGGCCTCCTTGATA
m_Acaca	GATGAACCATCTCCGTTGGC	GACCCAATTATGAATCGGGAGTG
m_Elovl6	GAGCAGAGGCGCAGAGAAC	ATGCCGACCACCAAAGATAA
m_Scd1	TTCTTGCGATACACTCTGGTGC	CGGGATTGAATGTTCTTGTCGT
m_Dgat2	GCGCTACTTCCGAGACTAC	GGGCCTTATGCCAGGAAACT
m_Adipoq	TGTTCCTCTTATCCTGCCCA	CCAACCTGCACAAGTTCCCTT
m_Cpt1a	CTCCGCCTGAGCCATGAAG	CACCAGTGATGATGCCATTCT
m_Ebi3	GCTCCCCTGGTTACACTGAA	ACGGGATACCGAGAAGCAT
m_p35	TCAGAATCACAACCATCAGCA	CGCCATTATGATTCAGAGACTG
H_Gapdh	CCATGAGAAGTATGACAACAG	GGGTGCTAAGCAGTTGGTG
H_P35	TGCCTTCACCACTCCCAAAACC	CAATCTCTTCAGAAGTGCAAGGG
H_EBI3	CTGGATCCGTTACAAGCGTCAG	CACTTGGACGTAGTACCTGGCT
Chemicals, Enzymes and other reagents		
Fast SYBR Green Master Mix	Applied Biosystems	Cat# 4385616
Protein marker PS10 Plus (5 × 500 µl)	Attenbio	Cat# PL-5
Purified NA/LE Hamster Anti-Mouse CD28 (clon 37.51)	BD Bioscience	Cat# 553294
BD Pharmingen™ Purified NA/LE Hamster Anti-Mouse CD3e (clon 145-2C11)	BD Bioscience	Cat# 553057
Ultra-LEAF™ Purified anti-human CD3 Antibody (clon OKT3)	Biolegend	Cat# 317326
Recombinant Human TGF-β1 (carrier-free)	BioLegend	Cat# 580702
Acrilamide	Bio-Rad	Cat# 161-0156
Rapamycin	Biorbyt	Cat# orb154705
EDTA	Calbiochem	Cat# 324503
MOPS-SDS running buffer (20X), 1 L	Fisher	Cat# 15435159
Amersham ECL Prime Western Blotting Detection Reagent	GE Healthcare	Cat# RPN2232
Ficoll-Paque PLUS*	GE Healthcare	Cat# 17-1440-03
Fetal Bovine Serum (FBS)	Gibco	Cat# 1027-106
L-Glutamine	Hyclone	Cat# SH30034.01
Amphotericin B (Fungizone) solution	Hyclone	Cat# SV30078.01
Hepes	Hyclone	SH30237.01
Non-essential amino acids	Hyclone	Cat# SH30238.01
Methanol	Honeywell	Cat# 24229
Tri reagent (Trizol)	Invitrogen	Cat# 15596-026
Insulin Humulina 100 UI/ml	Lilly	N/A
Ammonium Persulfate (APS)	Merck	Cat# 101200

Reagent/Resource	Reference or Source	Identifier or Catalog Number
β-mercaptoethanol	Merck	Cat# 805740
Bromophenol blue	Merck	Cat# 108122
NaF	Merck	Cat# B0590249
10% NEUTRAL BUFFERED FORMALIN	Proquinorte S.A.	Cat# BAF-0010-10X
Recombinant Human IL-2	Peprotech	Cat# 200-02
Aprotinin	Roche	Cat# 11583794001
Leupeptin	Roche	Cat# 11017128001
IL-35 EBI3 Mouse Recombinant Protein	Rockland	Cat# 010-001-B66
Dexamethasone	Sigma	Cat# D1756-100MG
3-isobutyl-1-methylxanthine	Sigma	Cat# I5879-250MG
Indomethacin	Sigma	Cat# I7378-100G
Insulin	Sigma	Cat# I9278
Ionomycin from Streptomyces conglobatus	Sigma	Cat# I9657-1MG
LIBERASE TL RESEARCH GRADE	Sigma	Cat# 5401020001
Ponceau	Sigma	Cat# P3504-10G
Bovine Serum Albumin	Sigma	Cat# A7906
Norepinephrine	Sigma	Cat# A7257-500MG
Na pyrophosphate	Sigma	Cat# 221368-100 G
Na orthovanadate	Sigma	Cat# S6508-10G
Sucrose	Sigma	Cat# S9378
Sodium dodecyl sulfate (SDS)	Sigma	Cat# L5750
PMSF	Sigma	Cat# P7626
Phorbol 12-myristate 13-acetate (PMA)	Sigma	Cat# P8139-1MG
Oil-Red	Sigma	Cat# O0625-25G
RPMI	Sigma	Cat# 21875-034
Hematoxylin	Sigma	Cat# H3136
Tween-20	Sigma	Cat# P1379-1L
DNase Type II-S	Sigma	Cat# D4513
Penicilin-Strepomicin	Sigma	Cat# P4333
T3 3,3′,5-Triiodo-L-Thyronine Free acid	Sigma	Cat# T2877-250MG
Temed	Sigma	Cat# T9281
Tissue-Tek® optimum cutting temperature (O.C.T.)	SAKURA FINETEK USA INC	Cat# 25608-930
Doramapimod (BIRB 796)	SELLECK CHEMICALS LLC	Cat# S1574
Adezmapimod (SB203580)	SELLECK CHEMICALS LLC	Cat# S1076
Troglitazone	Tocris Bioscience	Cat# 3114/10
HBSS, calcium, magnesium, no phenol red	Thermofisher	Cat# 14025-050
Eosin Y Alcoholic	Thermo Scientific	Cat# 6766008
Software		
GraphPad PRISM 7	GraphPad Software	RRID:SCR_002798
Photoshop CS6	Adobe	RRID:SCR_014199
Adobe Illustrator	Adobe	RRID:SCR_010279
Seahorse Wave	Agilent	N/A
FlowJo	FlowJo	https://www.flowjo.com/ RRID:SCR_008520
Fiji	ImageJ	RRID:SCR_002285
FlirIR software	FLIR	RRID:SCR_016330
METABOLISM Software	Panlab	Cat# 760817
Seurat 4.0	Satijalab	N/A
Sequence Detection System v2.4	Applied Biosystems	Cat# 4350490

Reagent/Resource	Reference or Source	Identifier or Catalog Number
Other		
Human buffy coats	Blood Transfusion Center of Comunidad de Madrid	N/A
Foxp3 Transcription Factor Staining Buffer Kit	eBioscience™,ThermoFisher	Cat# A25866A
EasySep™ Mouse Naive CD4 + T Cell Isolation Kit	StemCell Technologies	Cat# 19765
EasySep™ Human Naive CD4 + T Cell Isolation Kit II	StemCell Technologies	Cat# 17555
RNa easy Mini Kit	Qiagen	Cat# 74106
Zombie Aqua™ Fixable Viability Kit	BioLegend	Cat# 423101
DAPI (for nucleic acid staining)	Sigma	Cat# D9542-5MG
RNa easy Mini Kit	Qiagen	Cat# 74106
Rna easy Micro kit	Qiagen	Cat# 217084
High-Capacity cDNA Reverse Transcription Kit	Applied Biosystems	Cat# 4368814
Breeding & Maintenance diet for nude rats and mice and transgenic strains	Altromin	Cat# 1410
Glucometer	Ascensia Breeze 2 glucose meter	N/A
7900 Fast Real Time thermocycler	Applied Biosystems	
Glucose test strips Contour Next (50UN)	Bayer (Ascensia)	Cat# 84167836
Nitrocellulose Membrane (Pkg of 1 roll, 0.2 µm, 30 cm × 3.5 m)	Bio-Rad	Cat# 162-0112
Mini-PROTEAN® Tetra Vertical Electrophoresis Cell for Mini Precast Gels, 2-gel	Bio-Rad	Cat# 1658005
Mini Trans-Blot Module	Bio-Rad	Cat# 1703935
BD FACSymphony SORP	BD Bioscience	N/A
BD FACS Aria II SORP	BD Bioscience	RRID:SCR_018934
70 µM cell strainers	Corning Falcon	Cat# 352350
Paraffin embedding station	Leica Microsystems	EG 1150 H
Leica microscope	Leica Microsystems	Leica DM2500
Paraffin embedding station	Leica Microsystems	EG 1150 H
Tissue magnalyser	Roche	N/A
HFD with 60 kcal + 1.5% cholesterol	Research Diets Inc/BROGAARDEN	Cat# D11103002i
Metabolic cages	TSE LabMaster, TSE Systems, Germany	N/A
Small animal magnetic resonance scanner 7 Tesla	Varian-Agilent	N/A

Human visceral fat samples

For the analysis of visceral fat, the study population included 65 patients (52 adult patients with BMI > 35) recruited from patients who underwent elective bariatric surgery at the University Hospital of Salamanca. Patients were excluded if they had a history of alcohol use disorders or excessive alcohol consumption (>30 g/day in men and >20 g/day in women) or had chronic hepatitis C or B. Control subjects ($n = 12$) were recruited among patients who underwent laparoscopic cholecystectomy for gallstone disease. The patient data is presented in Table 1.

Study approval

Human peripheral blood mononuclear cells (PBMC) were isolated from buffy coats obtained from healthy donors according to standard procedures. Buffy coats of healthy donors were received from the Blood Transfusion Center of the Comunidad de Madrid, and all donors signed their consent for the use of samples for research purposes. All procedures using primary human cells were approved by the Ethics Committee of Hospital Universitario de la Princesa. For visceral fat samples the population study was approved by the Ethics Committee of the University Hospital of Salamanca and the Carlos III (CEI PI 09_2017-v3) with the all subjects providing written informed consent to undergo visceral fat biopsy under direct vision during surgery. Data were collected on demographic information (age, sex, and ethnicity), anthropomorphic measurements (BMI), smoking and alcohol history, coexisting medical conditions, and medication use. All animal procedures conformed to EU Directive 86/609/EEC and Recommendation 2007/526/EC regarding the protection of animals used for experimental and other scientific purposes, enacted under Spanish law 1 1201/2005. The protocols are CNIC-07/18 and PROEX 215/18.

Isolation, culture, and stimulation of human peripheral blood CD4⁺ T Cells

Human peripheral blood mononuclear cells (PBMC) were collected from buffy coats from healthy donors by Ficoll density gradient separation, as described (Schmidt et al, 2016). $CD4^+$ cells were isolated using the EasySep™ Human Naive $CD4^+$ T Cell Isolation Kit II. For in vitro Treg differentiation, isolated cells were activated with plate-bound anti-CD3 (3 µg/ml) and RPMI 1640 medium containing 10% FBS, 1% penicillin/streptomycin, 50 µM 2-mercaptoethanol, 2 mM L-glutamine, 1% non-essential AA, 1% anti-

Table 1. Characteristics of obese patients and controls for visceral fat analysis.

Variable	Obese patients ($n = 52$)	Controls ($n = 12$)	p
BMI (kg/m^2)	49.39 (7.39)	25.71 (3.64)	<0.0001
Body fat (%)	53.83 (4.13)	32.26 (8.30)	<0.0001
Fasting blood sugar (mg/dL)	114.04 (47.91)	94.73 (10.39)	0.191
Insulin (pmol/L)	978.49 (1722.735)	371.90 (433.92)	0.488
HOMA-IR	8.46 (25.09)	2.75 (3.64)	0.478
AST (IU/L)	24.61 (12.46)	21.45 (5.61)	0.415
ALT (IU/L)	32.60 (18.29)	24.73 (11.82)	0.178
Total cholesterol (mg/dL)	193.80 (39.05)	199.5 (43.82)	0.683
Triglycerides (mg/dL)	156.24 (88.95)	147.39 (56.12)	0.765
LDL-cholesterol (mg/dL)	113.81 (38.126)	121 (35.366)	0.604
HDL-cholesterol (mg/dL)	47.12 (13.11)	48.61 (18.84)	0.773

Variables are presented as mean (standard deviation) and analyzed by *t*-test.
BMI body mass index, *AST* aspartate aminotransferase, *ALT* alanine aminotransferase.

mycotic, 2.5 ng/ml TGF-b, and 50 U/ml IL-2 with or without 10 μM BIRB796 for 6 days in a humidified atmosphere (5% CO_2, 95% air) at 37 °C.

Mice

Floxed mutant mice for *Map2k6* (*Mkk6*) genes were as described (Matesanz et al, 2017). Mice with a germ-line mutation in the *Map2k3* gene and LoxP elements inserted into two introns (*Map2k3*LoxP) were generated after homologous recombination in ES cells, obtained from EUCOMM clon EPD0160_3_H09. The ES cell clones were injected into C57BL/6J blastocysts to create chimeric mice that transmitted the mutated *Map2k3* allele through the germ line. The Flp NeoR cassette was excised by crossing these mice with ACTB:FLPe B6;SJL mice, which express a FLP1 recombinase gene under the direction of the human ACTB promoter. These animals were crossed with Tg (CD4-cre)1Cwi/BfluJ mice on the C57BL/6J background (Jackson Laboratory) to generate mice lacking MKK3 and MKK6 in T cells (MKK3/6$^{CD4\text{-}KO}$). TSC1$^{CD4\text{-}KO}$ (Tsc1_lox (lox/lox) Tg.Cd4-Cre) were from Dr. Alejo Efeyan (CNIO). All mice were maintained on a C57BL/6J background (back-crossed for 10 generations). Genotype was confirmed by PCR analysis of genomic DNA. Mice were fed an ND or an HFD (Research Diets Inc.) for 2 weeks or 8–10 weeks ad libitum. As a control, we used age-matching either CD4-Cre mice or MKK3/6$^{f/f}$ (Cre negative) mice which is clearly indicated in results and figure legends. Mice were randomly assigned to cages, with inclusion or exclusion criteria based on instances of animal fights or harm during the study. Mice were housed at temperature standard for our animal facility (23–25 °C). For thermoneutrality experiments, mice were housed them at 30 °C and fed HFD for 4 or 8 weeks (until the end of the experiment). All analysts were blinded to experimental group or treatment.

BAT temperature measurement

BAT-adjacent interscapular temperature was quantified from thermographic images captured with a FLIR T430sc Infrared Camera (FLIR Systems, Inc., Wilsonville, OR) and analyzed with FLIR software.

NE administration

MKK3/6$^{CD4\text{-}KO}$ and MKK3/6$^{f/f}$ mice were housed at 30 °C and fed HFD for 4 weeks and then injected norepinephrine (NE 1 mg/kg of BW, i.p., Sigma-Aldrich). BAT-adjacent interscapular temperature was measured before the NE administration and 10 and 20 min after NE and quantified with FLIR software. In between capturing thermogenic images, mice were kept at 30 °C to avoid that room temperature affects BAT-adjacent interscapular temperature.

IL-35 administration

WT (C57BL6) mice were injected with IL-35 (300 ng/mouse, 010-001-B66, Rockland Immunochemicals, Inc.) or PBS i.v. in the retro-orbital sinus. 4 h later BAT-adjacent interscapular temperature was measured and quantified.

Isolation, culture, and in vitro induction of murine Treg cells

For in vitro Treg differentiation, naive CD4$^+$ T cells were isolated from the spleens of CD4-Cre, MKK3/6$^{CD4\text{-}KO}$, or TSC1$^{CD4\text{-}KO}$ mice using the EasySep™ Mouse Naive CD4$^+$ T Cell Isolation Kit, STEMCELL Technologies. Cells were plated on plates previously coated with 2 μg/mL anti-CD3 antibody and incubated with 2 μg/mL anti-CD28, 2 ng/mL TGF-β1 and 20 ng/mL IL-2 in RPMI1640 supplemented with 10% FBS, 1% penicillin/streptomycin, 50 μM 2-mercaptoethanol, 2 mM L-glutamine, and 1% antimycotic for 96 h in a humidified atmosphere (5% CO_2, 95% air) at 37 °C. At the end of the experiment, iTreg cells were collected for RNA and protein isolation or treated with rapamycin (100 nm) for 4 h and used for FACS analysis.

Real-time bioenergetic measurements in response to activation

We measured real-time naive CD4$^+$ T cells activation measurements by Seahorse XFe96 as described (van der Windt et al, 2016). In brief, naive CD4$^+$ T cells were isolated from the spleens of CD4-Cre and MKK3/6$^{CD4\text{-}KO}$ mice using the EasySep™ Mouse Naive CD4$^+$ T Cell Isolation Kit, STEMCELL Technologies. Cells were plated on Seahorse XFe96 plates previously coated with 50 μg/mL poly-L-lysine (Sigma) in DMEM containing 25 mM glucose, 2 mM L-glutamine and 1 mM sodium pyruvate and placed 1 h in non-CO_2 incubator at 37 °C. Cells were stimulated with 50 ng/ml of PMA and 500 ng/ml of Ionomycin which was injected after third measurement (the protocol was 3 min mix–2 min wait–3 min measure) and analyzed using Seahorse Wave software (Agilent).

Adipocyte in vitro differentiation and IL-35 stimulation

Immortalized brown preadipocytes from WT mice (mycoplasma free cells) were differentiated to brown adipocytes in 10% FCS medium supplemented with 20 nM insulin, 1 nM T3, 125 µM indomethacin, 2 µg/ml dexamethasone, and 50 mM IBMX for 48 h and maintained with 20 nM of insulin and 1 nM of T3 for 8 days. Primary white preadipocytes were isolated from C57BL/6 mice were differentiated to adipocytes for 9 days in 8% FCS medium supplemented with 5 µg/ml insulin, 25 µg/ml IBMX, 1 µg/ml dexamethasone, and 1 µM troglitazone (we changed medium every other day and supplemented with insulin and troglitazone, or the last changes were with insulin only). Differentiated adipocytes were stimulated in the presence or absence of 100 ng/ml IL-35 (010-001-B66, Rockland) for 0–2 h or for 48 h and then the cells were lysed for western blot. In some experiments we used 10 µM SB20253580 for 48 h together with IL-35.

Glucose measurement

Mice were starved overnight (fasted) or for 1 h (fed) and blood glucose levels were quantified with an Ascensia Breeze 2 glucose meter.

GTT

Overnight-starved mice were injected intraperitoneally with 1 g/kg of body weight of glucose, and blood glucose levels were quantified with an Ascensia Breeze 2 glucose meter at 0, 15, 30, 60, 90, and 120 min post injection.

ITT

ITT was performed by injecting intraperitoneally 0.75 IU/kg of insulin (Lilly) at mice starved for 1 h and detecting blood glucose levels with a glucometer at 0, 15, 30, 60, and 90 min post injection.

Indirect calorimetry system

Energy expenditure, respiratory exchange, locomotor activity, and food intake were quantified using the indirect calorimetry system (TSE LabMaster, TSE Systems, Germany) for 3 days.

Measurement of fecal lipids

Fecal lipids were extracted from dried feces (300 mg) collected from individually housed mice during 5 days according to Kraus D et al (Kraus et al, 2015). In brief, collected feces were dried overnight at 55 °C, and lipids were extracted by 2 ml chloroform : methanol (2:1) and using tissue magnalyser (Roche) followed by centrifugation 1000 × *g* for 10 min in plastic 15-ml falcon tubes. The lower phase containing lipids with chloroform and methanol were collected by carefully insertion of a 21 G needle through the tube wall into the lower, lipid phases and placed in a new 2 ml tubes (previously measured the weight of empty tubes). The tubes were left for 72 h at 37 °C until all liquid was evaporated and weighed again. The lipid content was measured by subtracting the weight of empty tubes to lipid mass per 300 mg of feces.

Nuclear magnetic resonance imaging analysis (MRI)

Body, fat, and lean mass were measured by nuclear magnetic resonance (Varian-Agilent, MA, USA) and analyzed with Fiji software (Image J).

Histology

Fresh livers, eWAT, sWAT, and BAT were fixed in 10% formalin, included in paraffin, and cut into 5 µm slides followed by haematoxylin–eosin staining. Fat droplets in liver were detected by oil-red staining (0.7% in propylenglycol) in 8 µm liver slides included in OCT compound (Tissue-Tek).

Tissue processing for flow cytometry

At the end of experiments, mouse axillar and inguinal lymph nodes, blood (100 µl), and spleens were collected, and single-cell suspensions were obtained by passing through a 70-µm cell strainer. Erythrocytes in pellets from all tissues (except lymph nodes) were lysed with a red cell lysis buffer, and the remaining cells were subsequently resuspended in flow cytometry buffer (2 PBS + 1% FBS + 2 mM EDTA). Epididymal white adipose tissue (eWAT) was carefully excised, minced, and digested with 1 mg/mL liberase + 2 U/ml DNAse in HBSS for 25-30 min at 37 °C with shaking at 1200 rpm. Digestion was stopped by addition of PBS + 10% FBS, and cells were passed through a 70-µm cell strainer and centrifuged for 5 min at 500 × *g* to obtain the stromal-vascular fraction (SVF). SVF pellets were also used for RNA isolation and subsequent qRT-PCR analysis.

Flow cytometry and cell sorting

Single-cell suspensions were stained with surface antibodies, and dead cells were excluded by nuclear staining with DAPI or Zombi Aqua™. Fluorochrome-conjugated antibodies to surface proteins were as follows: anti-CD45 V450 (clone 30-F11, BD Bioscience, Cat# 560501), anti-CD3 AF700 (clone 17A2, Biolegend, Cat# 141727), anti-CD4 APC-Cy7 (clone RM4-5, Biolgened, Cat# 100525), anti-CD8 BV785 (clone 53-6.7, Biolegend, Cat# 100749), anti-CD8 BV510 (clone: 53-6.7), anti-CD25 PE (clone PC61, Biolegend, Cat# 102007), anti-CD25 BV421 (clone: A18246A, Biolegend, Cat# 113705), anti-CD206 BV711 (clone C068C2, Biolegend, Cat# 141727), anti-F4/80 AF647 (clone Cl:A3-1, BioRad, Cat# MCA497A647), anti-F4/80 PE-Cy7 (clone: BM8, Thermofisher, Cat# 25-4801-82), anti-CD11b FITC (clone M1/70, BD Bioscience, Cat# 557396), anti-CD11b BV785 (clone: M1/70, Biolegend, Cat# 101243), anti-CD11c PE (clone HL3, BD Bioscience, Cat# 553802), anti-IL-35 PE (clone 27537, Thermofisher, Cat# MA5-23559), and anti-NK1.1 PerCP-Cy5.5 (clone PK136, Biolegend, Cat# 108728). For intranuclear staining, cells were fixed and permeabilized with the eBioscience Foxp3 Transcription Factor Staining Buffer Kit followed by anti-Foxp3 APC (clone FJK-16s) or anti-Foxp3 FITC (clone FJK-16s) staining. For intracellular staining of IL-35, cells were activated with PMA/ionomycin/Brefeldin A for hours before surface staining. After staining, cells were passed through 70 µm filters, and data were acquired with a BD FACSymphony flow cytometer and analyzed

with FlowJo software. The gating strategy is presented in Appendix Fig. S4A,B.

Single-cell suspensions of splenocytes from mice were stained with the following surface antibodies: anti-CD4 APC-Cy7 (clone RM4-5), anti-CD8 BV785 (clone 53-6.7), anti-CD3 AF700 (clone 17A2), anti-CD11b FITC (clone M1/70), and anti-CD45 V450 (clone 30-F11). Nuclei were stained with DAPI to distinguish live and dead cells. Cells were sorted with a BD FACS Aria cell sorter into the following populations: $CD4^+$ T cells ($CD45^+CD3^+CD4^+CD8^-$), $CD8^+$ T cells ($CD45^+CD3^+CD8^+CD4^-$) and NK cells ($CD45^+NK1.1^+CD3^-$). Sorted cells were collected, lysed, and analyzed by western blot to check MKK3 and MKK6 deletion.

Western blot

Samples were lysed in Triton lysis buffer [20 mM Tris (pH 7.4), 1% Triton X-100, 10% glycerol, 137 mM NaCl, 2 mM EDTA, 25 mM β-glycerophosphate, 1 mM sodium orthovanadate, 1 mM phenylmethylsulphonyl fluoride, and 10 µg/mL aprotinin, and leupeptin]. Extracts (20–50 µg protein) were examined by immunoblot. Primary antibodies used in the study: anti-mouse MKK3 (Cat# 9238, Cell Signaling Technology), anti-mouse MKK6 (Cat# ADI-KAP-MA014-E, Enzo Life Sciences), anti-mouse UCP1 (Cat# AB10983, Abcam), anti-mouse FGF21 (Cat# RD281108100, BioVendor), anti-mouse p-ATF2 T69/71 (Cat# 9225S, Cell Signaling Technology), anti-mouse ATF2 (Cat# 9226S, Cell Signaling Technology), anti-mouse p-s6 S240/244 (Cat# 5364S, Cell Signaling Technology), anti-mouse p-p38 T180/Y182 (Cat# 9211S, Cell Signaling Technology), anti-mouse b-actin (Cat# sc-47778, Santa Cruz Technology), anti-mouse vinculin (Cat# V9131, Sigma) and secondary antibodies used in the study: goat anti-mouse (Cat# 31430, ThermoFisher) and goat anti-rabbit (Cat# 31460, ThermoFisher). Reactive bands were detected by chemiluminescence.

qRT-PCR

RNA (1 µg) extracted with the RNeasy Plus Mini kit or RNeasy Plus Micro kit (Quiagen) was transcribed to cDNA, and qRT-PCR was performed using the Fast Sybr Green probe (Applied Biosystems) and the appropriate primers in a 7900 Fast Real Time thermocycler (Applied Biosystems). Data were analyzed with SDS2.4 software (Applied Biosystems), and relative mRNA expression was normalized to *GAPDH* (human data) or *b-actin* (mouse data) mRNA measured in each sample. Primers used are listed in the reagents table.

Single-cell RNA-Seq processing

Single-cell RNA sequencing data from human WAT was obtained from Emont et al (Emont et al, 2022) (https://gitlab.com/rosen-lab/white-adipose-atlas). The Seurat RDS file for immune cells was downloaded and processed with Seurat 4.0 (Hao et al, 2021) (https://satijalab.org/seurat/). The clusters of T cells and Treg cells were subset and exported for further analysis. As the clusters were already identified, integration was not re-run, but we applied a linear transformation to scale the data from the T cells and Treg cells isolated cluster, followed by dimension reduction analysis (PCA). Following PCA analysis, the first 20 and 30 dimensions were used for further analysis in the T cells and Treg cells, respectively. We performed non-linear dimension reduction analysis using the UMAP algorithm. The analysis was done using the first 20 and 30 dimensions for the T cells and Treg cells clusters, respectively, and a resolution of 0.5. Differentially expressed genes between BMI ranges were identified with a non-parametric Wilcoxon rank sum test.

Statistical analysis

Results are expressed as mean ± SEM. Statistical differences were analyzed by the Student *t* test or 2-way ANOVA, with differences at $p < 0.05$ considered significant. When variances were different, ANOVA coupled with Bonferroni's post-tests. When variances were different in *t* test, we used Welch's test. All analyses were performed with Excel (Microsoft Corp.) and GraphPad PRISM 7 software. Statistical details for individual the experiments were indicated in the figure legends.

Data availability

No primary datasets have been generated and deposited.

The source data of this paper are collected in the following database record: biostudies:S-SCDT-10_1038-S44319-024-00149-y.

Expanded view data, supplementary information, appendices are available for this paper at https://doi.org/10.1038/s44319-024-00149-y.

Peer review information

A peer review file is available at https://doi.org/10.1038/s44319-024-00149-y

References

Bapat SP, Myoung Suh J, Fang S, Liu S, Zhang Y, Cheng A, Zhou C, Liang Y, LeBlanc M, Liddle C et al (2015) Depletion of fat-resident Treg cells prevents age-associated insulin resistance. Nature 528:137–141

Beppu LY, Mooli RGR, Qu X, Marrero GJ, Finley CA, Fooks AN, Mullen ZP, Frias Jr. AB, Sipula I, Xie B et al (2021) Tregs facilitate obesity and insulin resistance via a Blimp-1/IL-10 axis. JCI Insight 6:e140644

Burzyn D, Benoist C, Mathis D (2013) Regulatory T cells in nonlymphoid tissues. Nat Immunol 14:1007–1013

Cao W, Daniel KW, Robidoux J, Puigserver P, Medvedev AV, Bai X, Floering LM, Spiegelman BM, Collins S (2004) p38 mitogen-activated protein kinase is the central regulator of cyclic AMP-dependent transcription of the brown fat uncoupling protein 1 gene. Mol Cell Biol 24:3057–3067

Cereijo R, Gavaldà-Navarro A, Cairó M, Quesada-López T, Villarroya J, Morón-Ros S, Sánchez-Infantes D, Peyrou M, Iglesias R, Mampel T et al (2018) CXCL14, a brown adipokine that mediates brown-fat-to-macrophage communication in thermogenic adaptation. Cell Metab 28:750–763.e756

Cipolletta D, Feuerer M, Li A, Kamei N, Lee J, Shoelson SE, Benoist C, Mathis D (2012) PPAR-gamma is a major driver of the accumulation and phenotype of adipose tissue Treg cells. Nature 486:549–553

Collison LW, Workman CJ, Kuo TT, Boyd K, Wang Y, Vignali KM, Cross R, Sehy D, Blumberg RS, Vignali DA (2007) The inhibitory cytokine IL-35 contributes to regulatory T-cell function. Nature 450:566–569

Crespo M, Gonzalez-Teran B, Nikolic I, Mora A, Folgueira C, Rodriguez E, Leiva-Vega L, Pintor-Chocano A, Fernandez-Chacon M, Ruiz-Garrido I et al (2020) Neutrophil infiltration regulates clock-gene expression to organize daily hepatic metabolism. Elife 9:e59258

Crespo M, Nikolic I, Mora A, Rodriguez E, Leiva-Vega L, Pintor-Chocano A, Horrillo D, Hernandez-Cosido L, Torres JL, Novoa E et al (2023) Myeloid p38 activation maintains macrophage-liver crosstalk and BAT thermogenesis through IL-12-FGF21 axis. Hepatology 77:874–887

Emont MP, Jacobs C, Essene AL, Pant D, Tenen D, Colleluori G, Di Vincenzo A, Jorgensen AM, Dashti H, Stefek A et al (2022) A single-cell atlas of human and mouse white adipose tissue. Nature 603:926–933

Enerbäck S, Jacobsson A, Simpson EM, Guerra C, Yamashita H, Harper ME, Kozak LP (1997) Mice lacking mitochondrial uncoupling protein are cold-sensitive but not obese. Nature 387:90–94

Fang W, Deng Z, Benadjaoud F, Yang D, Yang C, Shi GP (2020) Regulatory T cells promote adipocyte beiging in subcutaneous adipose tissue. FASEB J 34:9755–9770

Feuerer M, Herrero L, Cipolletta D, Naaz A, Wong J, Nayer A, Lee J, Goldfine AB, Benoist C, Shoelson S et al (2009) Lean, but not obese, fat is enriched for a unique population of regulatory T cells that affect metabolic parameters. Nat Med 15:930–939

Fisher FM, Kleiner S, Douris N, Fox EC, Mepani RJ, Verdeguer F, Wu J, Kharitonenkov A, Flier JS, Maratos-Flier E et al (2012) FGF21 regulates PGC-1alpha and browning of white adipose tissues in adaptive thermogenesis. Genes Dev 26:271–281

Gonzalez-Teran B, Cortes JR, Manieri E, Matesanz N, Verdugo A, Rodriguez ME, Gonzalez-Rodriguez A, Valverde AM, Martin P, Davis RJ et al (2013) Eukaryotic elongation factor 2 controls TNF-alpha translation in LPS-induced hepatitis. J Clin Invest 123:164–178

Gonzalez-Teran B, Lopez JA, Rodriguez E, Leiva L, Martinez-Martinez S, Bernal JA, Jimenez-Borreguero LJ, Redondo JM, Vazquez J, Sabio G (2016a) p38gamma and delta promote heart hypertrophy by targeting the mTOR-inhibitory protein DEPTOR for degradation. Nat Commun 7:10477

Gonzalez-Teran B, Matesanz N, Nikolic I, Verdugo MA, Sreeramkumar V, Hernandez-Cosido L, Mora A, Crainiciuc G, Saiz ML, Bernardo E et al (2016b) p38gamma and p38delta reprogram liver metabolism by modulating neutrophil infiltration. EMBO J 35:536–552

Hao Y, Hao S, Andersen-Nissen E, Mauck 3rd WM, Zheng S, Butler A, Lee MJ, Wilk AJ, Darby C, Zager M et al (2021) Integrated analysis of multimodal single-cell data. Cell 184:3573–3587.e3529

Hayakawa M, Hayakawa H, Petrova T, Ritprajak P, Sutavani RV, Jimenez-Andrade GY, Sano Y, Choo MK, Seavitt J, Venigalla RK et al (2017) Loss of functionally redundant p38 isoforms in T cells enhances regulatory T cell induction. J Biol Chem 292:1762–1772

Huber S, Schrader J, Fritz G, Presser K, Schmitt S, Waisman A, Lüth S, Blessing M, Herkel J, Schramm C (2008) P38 MAP kinase signaling is required for the conversion of CD4+CD25- T cells into iTreg. PLoS ONE 3:e3302

Ilan Y, Maron R, Tukpah AM, Maioli TU, Murugaiyan G, Yang K, Wu HY, Weiner HL (2010) Induction of regulatory T cells decreases adipose inflammation and alleviates insulin resistance in ob/ob mice. Proc Natl Acad Sci USA 107:9765–9770

Kalin S, Becker M, Ott VB, Serr I, Hosp F, Mollah MMH, Keipert S, Lamp D, Rohner-Jeanrenaud F, Flynn VK et al (2017) A Stat6/Pten axis links regulatory T cells with adipose tissue function. Cell Metab 26:475–492.e477

Khan IM, Dai Perrard XY, Perrard JL, Mansoori A, Wayne Smith C, Wu H, Ballantyne CM (2014) Attenuated adipose tissue and skeletal muscle inflammation in obese mice with combined CD4+ and CD8+ T cell deficiency. Atherosclerosis 233:419–428

Kohlgruber AC, Gal-Oz ST, LaMarche NM, Shimazaki M, Duquette D, Koay HF, Nguyen HN, Mina AI, Paras T, Tavakkoli A et al (2018) γδ T cells producing interleukin-17A regulate adipose regulatory T cell homeostasis and thermogenesis. Nat Immunol 19:464–474

Kraus D, Yang Q, Kahn BB (2015) Lipid extraction from mouse feces. Bio Protoc 5:e1375

Kuma Y, Sabio G, Bain J, Shpiro N, Marquez R, Cuenda A (2005) BIRB796 inhibits all p38 MAPK isoforms in vitro and in vivo. J Biol Chem 280:19472–19479

Lee MW, Odegaard JI, Mukundan L, Qiu Y, Molofsky AB, Nussbaum JC, Yun K, Locksley RM, Chawla A (2015) Activated type 2 innate lymphoid cells regulate beige fat biogenesis. Cell 160:74–87

Leiva M, Matesanz N, Pulgarín-Alfaro M, Nikolic I, Sabio G (2020) Uncovering the role of p38 family members in adipose tissue physiology. Front Endocrinol 11:572089

Li C, Wang G, Sivasami P, Ramirez RN, Zhang Y, Benoist C, Mathis D (2021) Interferon-α-producing plasmacytoid dendritic cells drive the loss of adipose tissue regulatory T cells during obesity. Cell Metab 33:1610–1623.e1615

Matesanz N, Bernardo E, Acin-Perez R, Manieri E, Perez-Sieira S, Hernandez-Cosido L, Montalvo-Romeral V, Mora A, Rodriguez E, Leiva-Vega L et al (2017) MKK6 controls T3-mediated browning of white adipose tissue. Nat Commun 8:856

Mathis D (2013) Immunological goings-on in visceral adipose tissue. Cell Metab 17:851–859

Matsumoto A, Taniguchi K, Takeda N, Yamamura KI, Arai S, Miyazaki T (2017) Inflammatory and anti-inflammatory states of adipose tissue in transgenic mice bearing a single TCR. Int Immunol 29:21–30

Moysidou M, Karaliota S, Kodela E, Salagianni M, Koutmani Y, Katsouda A, Kodella K, Tsakanikas P, Ourailidou S, Andreakos E et al (2018) CD8+ T cells in beige adipogenesis and energy homeostasis. JCI Insight 3:e95456

Nikolic I, Leiva M, Sabio G (2020) The role of stress kinases in metabolic disease. Nat Rev Endocrinol 16:697–716

Nishimura S, Manabe I, Nagasaki M, Eto K, Yamashita H, Ohsugi M, Otsu M, Hara K, Ueki K, Sugiura S et al (2009) CD8+ effector T cells contribute to macrophage recruitment and adipose tissue inflammation in obesity. Nat Med 15:914–920

Reilly SM, Abu-Odeh M, Ameka M, DeLuca JH, Naber MC, Dadpey B, Ebadat N, Gomez AV, Peng X, Poirier B et al (2021) FGF21 is required for the metabolic benefits of IKKepsilon/TBK1 inhibition. J Clin Invest 131:e145546

Risco A, Martin-Serrano MA, Barber DF, Cuenda A (2018) p38gamma and p38delta are involved in T lymphocyte development. Front Immunol 9:65

Sakaguchi S, Miyara M, Costantino CM, Hafler DA (2010) FOXP3+ regulatory T cells in the human immune system. Nat Rev Immunol 10:490–500

Sakamoto T, Nitta T, Maruno K, Yeh YS, Kuwata H, Tomita K, Goto T, Takahashi N, Kawada T (2016) Macrophage infiltration into obese adipose tissues suppresses the induction of UCP1 level in mice. Am J Physiol Endocrinol Metab 310:E676–e687

Saltiel AR, Olefsky JM (2017) Inflammatory mechanisms linking obesity and metabolic disease. J Clin Invest 127:1–4

Schipper HS, Prakken B, Kalkhoven E, Boes M (2012) Adipose tissue-resident immune cells: key players in immunometabolism. Trends Endocrinol Metab 23:407–415

Schmidt A, Éliás S, Joshi RN, Tegnér J (2016) In vitro differentiation of human CD4+FOXP3+ induced regulatory T cells (iTregs) from naïve CD4+ T cells using a TGF-β-containing protocol. J Vis Exp (118);55015. https://doi.org/10.3791/55015

Takeuchi Y, Nishikawa H (2016) Roles of regulatory T cells in cancer immunity. Int Immunol 28:401–409

van der Windt GJ, Chang CH, Pearce EL (2016) Measuring bioenergetics in T cells using a seahorse extracellular flux analyzer. Curr Protoc Immunol 113:3.16b.11–13.16b.14

Vijay J, Gauthier MF, Biswell RL, Louiselle DA, Johnston JJ, Cheung WA, Belden B, Pramatarova A, Biertho L, Gibson M et al (2020) Single-cell analysis of human adipose tissue identifies depot and disease specific cell types. Nat Metab 2:97–109

Wang Q, Li D, Cao G, Shi Q, Zhu J, Zhang M, Cheng H, Wen Q, Xu H, Zhu L et al (2021) IL-27 signalling promotes adipocyte thermogenesis and energy expenditure. Nature 600:314–318

Wing K, Sakaguchi S (2010) Regulatory T cells exert checks and balances on self tolerance and autoimmunity. Nat Immunol 11:7–13

Zhang X, Fan L, Wu J, Xu H, Leung WY, Fu K, Wu J, Liu K, Man K, Yang X et al (2019) Macrophage p38alpha promotes nutritional steatohepatitis through M1 polarization. J Hepatol 71:163–174

Zhang X, Huang T, Wu Y, Peng W, Xie H, Pan M, Zhou H, Cai B, Wu Y (2017) Inhibition of the PI3K-Akt-mTOR signaling pathway in T lymphocytes in patients with active tuberculosis. Int J Infect Dis 59:110–117

Acknowledgements

We thank S Bartlett for English editing and F Sanchez Madrid for providing human buffy coats. We thank the staff at the CNIC Cellomics and Advanced Imaging units for technical support and help with data analysis. IN was funded by EFSD/Lilly grants (2017 and 2019), the CNIC IPP FP7 Marie Curie Programme (PCOFUND-2012-600396), an EFSD Rising Star award (2019), and grant MINECO IJC2018-035390-I. IR FPI-MCIN PRE2020-092784. MC was an FPI-MINECO fellow (BES-2017-079711). RRB is a fellow of the FPU Program (FPU17/03847). ML was supported by Spanish grant MINECO-FEDER SAF2015-74112-JIN and Fundación AECC: INVES20026LEIV. ABP-G MG was awarded with FPI BES-2017 − 081381. JV was supported by MICIU/AEI/10.13039/501100011033 and by European Union (grants PID2021-122348NB-I00, PLEC2022-009298, PLEC2022-009235 and EQC2021-007053-P), by the Comunidad de Madrid (S2022/BMD-7333-CM), and by "La Caixa" Foundation (LCF/PR/HR22/52420019). MM has been funded by Instituto de Salud Carlos III (ISCIII) through the project PI20/00743 and INT21/00065 to MM and co-funded by the European Union and by Junta de Castilla y León, Spain through projects GRS 2388/A/21 and GRS 2648/A/22 to MM. PM is supported by MICIN-ISCIII-Fondo de Investigación Sanitaria (PI22/01759; PMPTA22/00090-BIOCARDIOTOX) and Comunidad de Madrid (P2022/BMD-7209-INTEGRAMUNE-CM; Spain). GS is a EMBO YIP member, received funding from the following programs and organizations: MCIN PGC2018-097019-B-I00; European Union Seventh Framework Programme (FP7/2007-2013) under grant agreement ERC 260464; the EFSD/Lilly European Diabetes Research Programme; Fundación AECC PROYE19047SABI; BBVA Foundation Leonardo Grants Program for Researchers and Cultural Creators (Investigadores-BBVA-2017) IN[17]_BBM_BAS_0066; MINECO-FEDER SAF2016-79126-R and PID2019-104399RB-I00, MICIN-FEDER PID2022-138525OB-I00 2023-26; and the Comunidad de Madrid (IMMUNOTHERCAN-CM S2010/BMD-2326 and B2017/BMD-3733), PMP21/00057. GS. MM, JV, JT has been awarded with Infraestructura de Medicina de Precisión asociada a la Ciencia y Tecnología IMPACT-2021 PMP21/00113. Instituto de Salud Carlos III., PDC2021-121147-I00.Convocatoria: Proyectos Prueba de Concepto 2021. Ministerio de Ciencia e Innovación. The CNIC is supported by the Instituto de Salud Carlos III (ISCIII), the Ministerio de Ciencia e Innovación (MCIN) and the Pro CNIC Foundation), and is a Severo Ochoa Center of Excellence (grant CEX2020-001041-S funded by MICIN/AEI/10.13039/501100011033).

Author contributions

Ivana Nikolic: Conceptualization; Resources; Data curation; Formal analysis; Supervision; Funding acquisition; Validation; Investigation; Visualization; Methodology; Writing—original draft; Writing—review and editing. **Irene Ruiz-Garrido**: Resources; Data curation; Formal analysis; Supervision; Validation; Investigation; Visualization; Methodology; Writing—original draft; Writing—review and editing. **María Crespo**: Data curation; Formal analysis; Supervision; Validation; Investigation; Visualization; Methodology; Writing—review and editing. **Rafael Romero-Becerra**: Data curation; Formal analysis; Supervision; Validation; Investigation; Visualization; Methodology; Writing—review and editing. **Luis Leiva-Vega**: Investigation; Methodology; Writing—review and editing. **Alfonso Mora**: Data curation; Formal analysis; Supervision; Validation; Investigation; Visualization; Methodology; Writing—review and editing. **Marta León**: Investigation; Methodology; Writing—review and editing. **Elena Rodríguez**: Investigation; Methodology; Writing—review and editing. **Magdalena Leiva**: Data curation; Formal analysis; Supervision; Validation; Investigation; Visualization; Methodology; Writing—review and editing. **Ana Belén Plata-Gómez**: Resources; Data curation; Formal analysis; Supervision; Validation; Investigation; Visualization; Methodology; Writing—review and editing. **Maria Beatriz Alvarez Flores**: Resources; Formal analysis; Validation; Investigation; Visualization; Methodology; Writing—review and editing. **Jorge L Torres**: Resources; Data curation; Formal analysis; Supervision; Validation; Investigation; Visualization; Methodology; Writing—review and editing. **Lourdes Hernández-Cosido**: Resources; Data curation; Formal analysis; Supervision; Validation; Investigation; Visualization; Methodology; Writing—review and editing. **Juan Antonio López**: Resources; Data curation; Formal analysis; Supervision; Validation; Visualization; Methodology; Writing—review and editing. **Jesús Vázquez**: Resources; Data curation; Formal analysis; Supervision; Funding acquisition; Validation; Investigation; Visualization; Methodology; Writing—review and editing. **Alejo Efeyan**: Resources; Data curation; Formal analysis; Supervision; Funding acquisition; Validation; Investigation; Visualization; Methodology; Writing—review and editing. **Pilar Martin**: Resources; Formal analysis; Supervision; Funding acquisition; Investigation; Visualization; Methodology; Writing—review and editing. **Miguel Marcos**: Resources; Data curation; Formal analysis; Supervision; Funding acquisition; Validation; Investigation; Visualization; Methodology; Project administration; Writing—review and editing. **Guadalupe Sabio**: Conceptualization; Resources; Data curation; Formal analysis; Supervision; Funding acquisition; Validation; Investigation; Visualization; Methodology; Writing—original draft; Project administration; Writing—review and editing.

Source data underlying figure panels in this paper may have individual authorship assigned. Where available, figure panel/source data authorship is listed in the following database record: biostudies:S-SCDT-10_1038-S44319-024-00149-y.

Disclosure and competing interests statement

The authors declare no competing interests.

Expanded View Figures

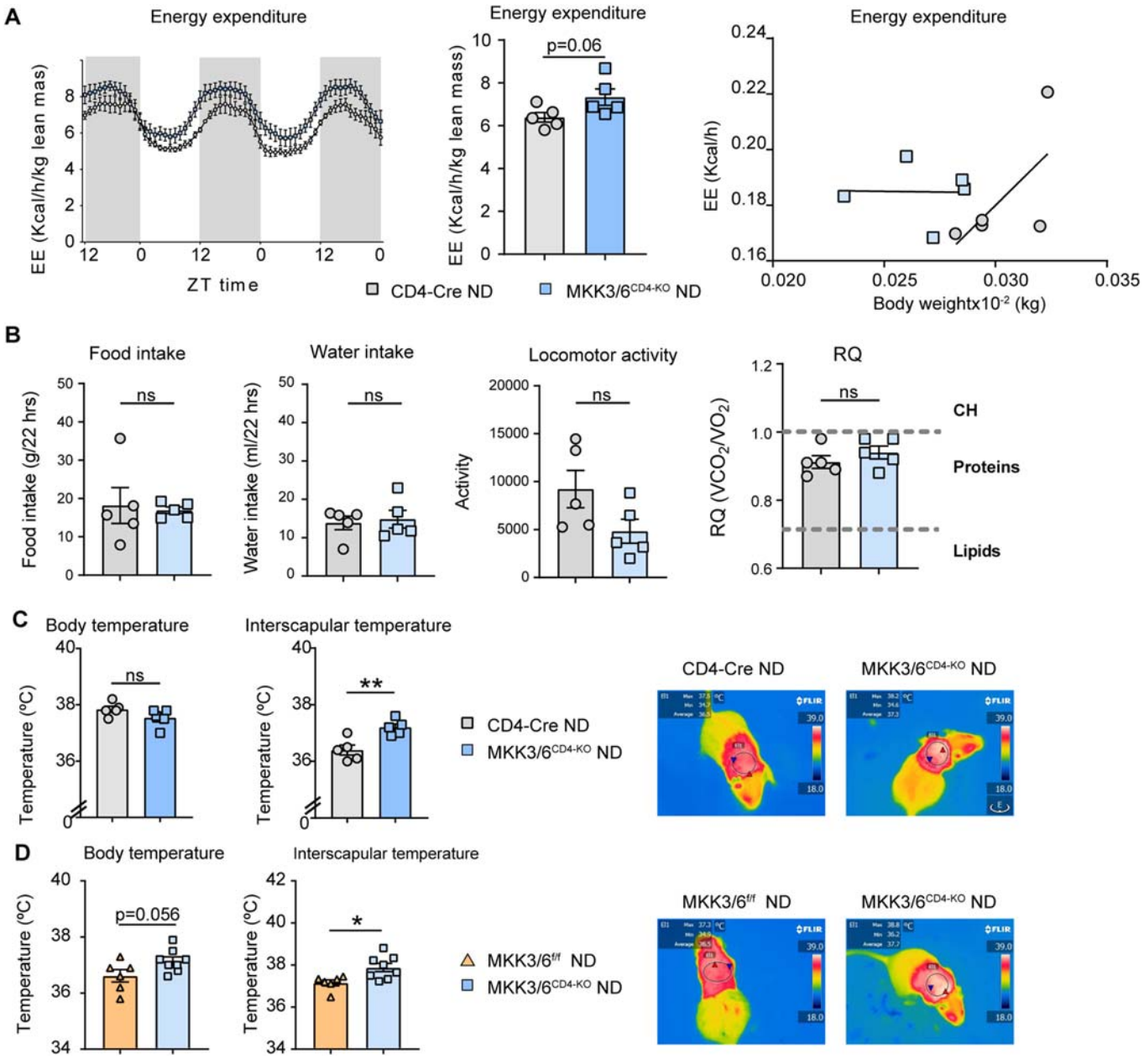

Figure EV1. MKK3/6 deficiency in T cells increases energy expenditure and BAT temperature.

(**A**) Comparison of energy balance between ND-fed MKK3/6$^{CD4\text{-}KO}$ and CD4-Cre mice examined in a metabolic cage over a 3-day period. Hour-by-hour lean-mass-corrected variation in energy expenditure (EE) (left panel); mean lean-mass-corrected EE (middle panel); and ANCOVA analysis of EE (kcal/h) (right panel). (**B**) Food and water intake, locomotor activity, and respiratory quotient obtained from metabolic cages. (**C**, **D**) Body temperature and skin temperature surrounding interscapular BAT. Right panels show representative infrared thermal images in (**C**) CD4-Cre and MKK3/6 $^{CD4\text{-}KO}$ mice and (**D**) in littermates (MKK3/6$^{f/f}$) and MKK3/6$^{CD4\text{-}KO}$ mice fed chow diet. Data information: Data are presented as mean ± SEM, *$p < 0.05$, **$p < 0.01$, ns: not significant. Exact *p*-values are shown. Analysis by 2-way ANOVA coupled to the Sidak's multiple comparison post-test (**A**) or by *t* test or by the Welch test when variances were different (**B–D**). $n = 5$–8 biologically independent mice for each group, represented as single dots in the graphs (**A–D**). Source data are available online for this figure.

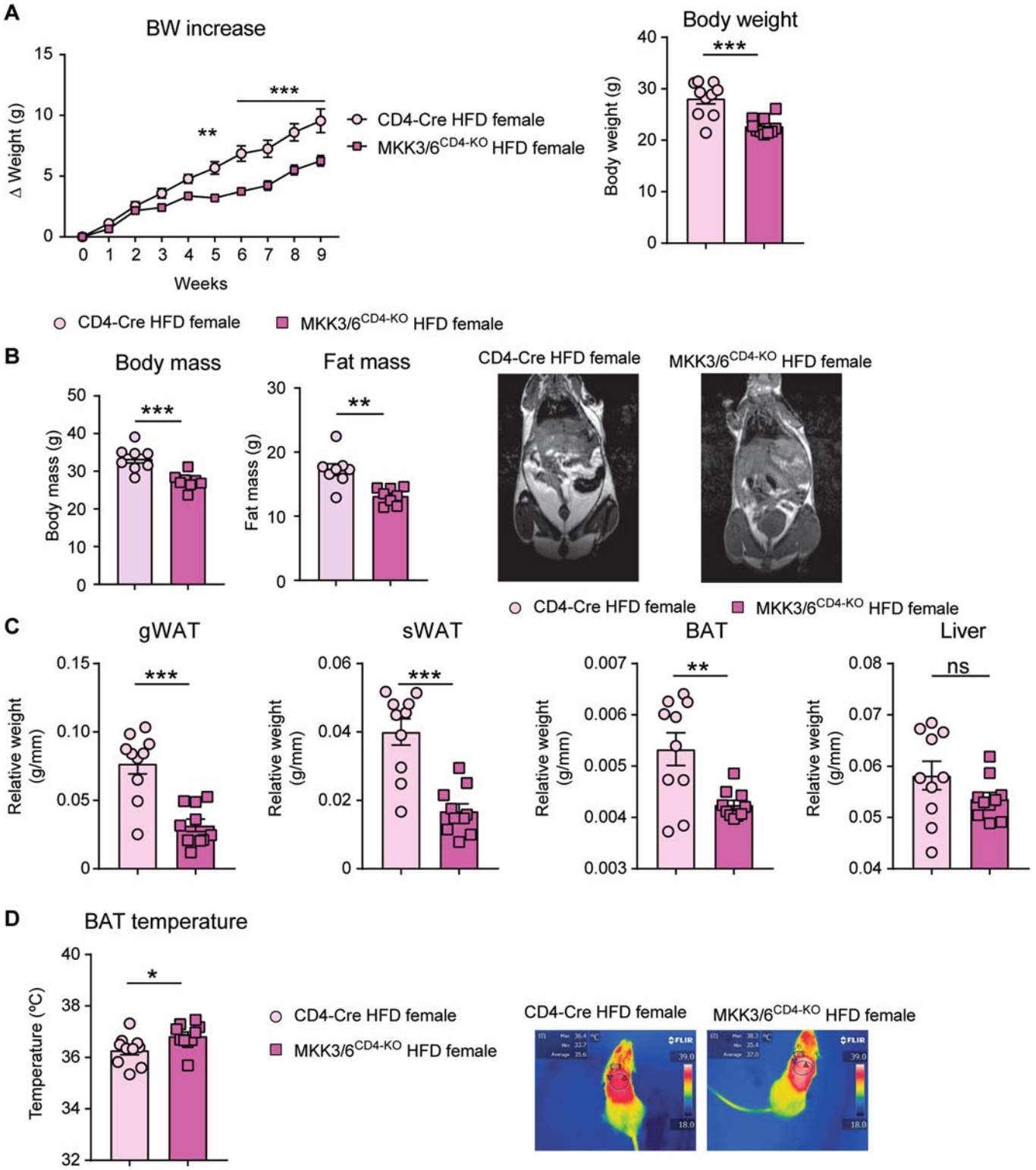

Figure EV2. MKK3/6 deficiency in T cells protects females against HFD-induced obesity.

(**A–D**) Female MKK3/6$^{CD4\text{-}KO}$ and CD4-Cre mice were fed a high-fat diet (HFD) for 9 weeks (starting at 8–10 weeks old). (**A**) Body weight evolution in MKK3/6$^{CD4\text{-}KO}$ and CD4-Cre female mice for 9 weeks. Data are presented as the increase above initial weight (left) and absolute weight at the end of the experiment (right). (**B**) MRI analysis of body and fat mass in MKK3/6$^{CD4\text{-}KO}$ and CD4-Cre mice after 8 weeks of HFD. Representative images are shown on the right. (**C**) eWAT, sWAT, BAT, and liver mass relative to tibia length. (**D**) Skin temperature surrounding interscapular BAT. Right panels show representative infrared thermal images. Data Information: Data are presented as mean ± SEM, $*p < 0.05$, $**p < 0.01$, $***p < 0.001$, ns: not significant. Analysis by 2-way ANOVA coupled to the Bonferroni post-test (**A**) or *t* test or by the Welch test when variances were different (**A–D**). $n = 8$–10 biologically independent mice for each group, represented as single dots in the graphs (**A–D**). Source data are available online for this figure.

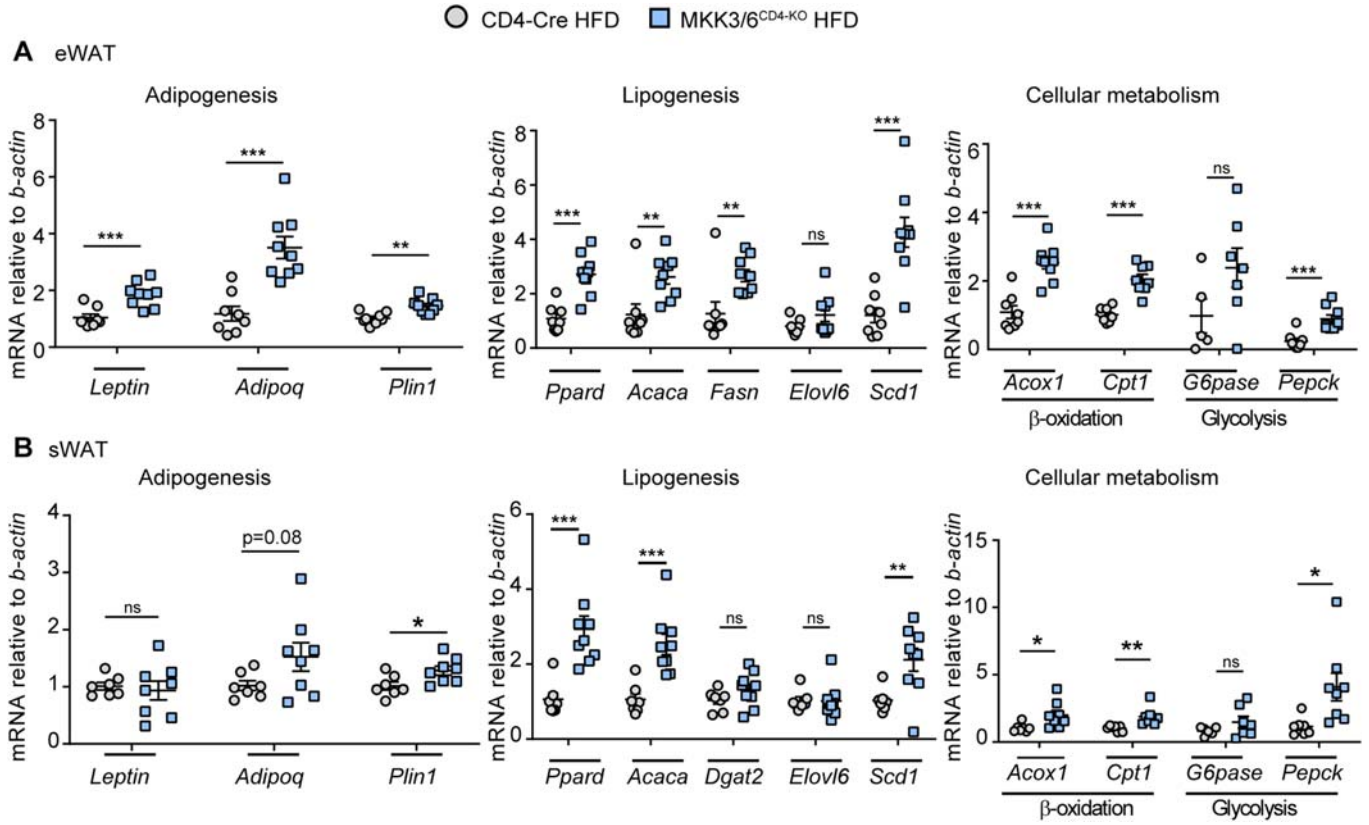

Figure EV3. Lack of MKK3/6 in T improves adipose tissue metabolic homeostasis.

(**A**, **B**) MKK3/6$^{CD4\text{-}KO}$ and control CD4-Cre mice were fed an HFD for 8 weeks. qRT-PCR analysis of adipogenic, lipogenic, β-oxidation, and glycolytic genes mRNA expression from (**A**) eWAT and (**B**) sWAT isolated from control CD4-Cre or MKK3/6$^{CD4\text{-}KO}$ mice. mRNA expression was normalized to the amount of *b-actin* mRNA. Data Information: Data are presented as mean ± SEM, *$p < 0.05$, **$p < 0.01$, ***$p < 0.001$, ns: not significant. Exact *p* values are shown. Analysis by *t* test or Welch's test when variances were different. $n = 8$-9 biologically independent mice for each group, represented as single dots in the graphs. Source data are available online for this figure.

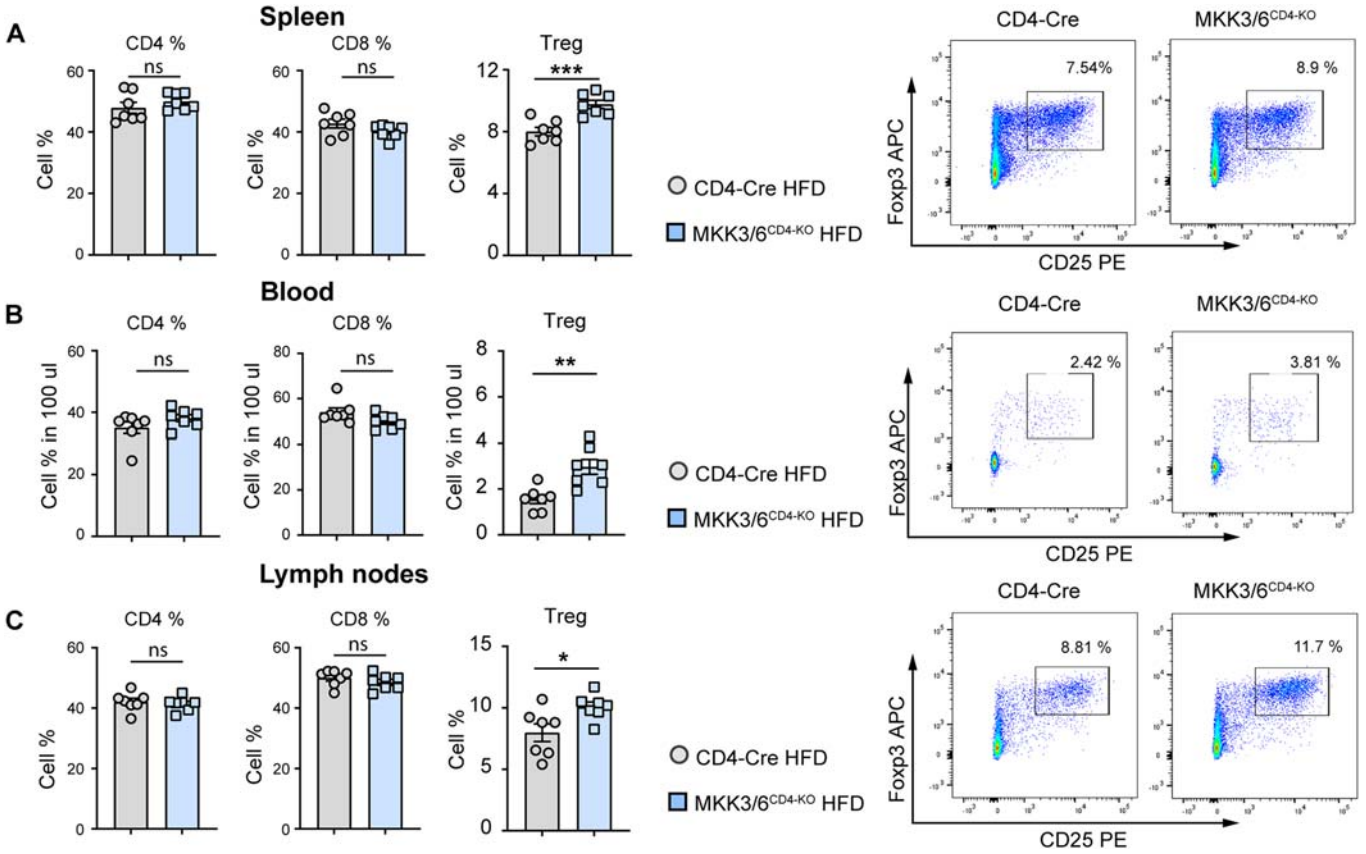

Figure EV4. MKK3/6 deletion in T cells increases Treg cell population in blood and lymph nodes.

(**A–C**) MKK3/6$^{CD4\text{-}KO}$ and CD4-Cre mice were fed a high-fat diet (HFD) for 8 weeks. FACS quantification and representative dot plots of CD4$^+$, CD8$^+$ and Treg cells (CD4$^+$CD25$^+$Foxp3$^+$) in spleen (**A**), blood (**B**), and lymph nodes (**C**). Data Information: Data are presented as mean ± SEM, $*p < 0.05$, $**p < 0.01$, $***p < 0.001$, ns: not significant. Analysis by *t* test or Welch's test when variances were different. $n = 7$ biologically independent mice for each group, represented as single dots in the graphs. Source data are available online for this figure.

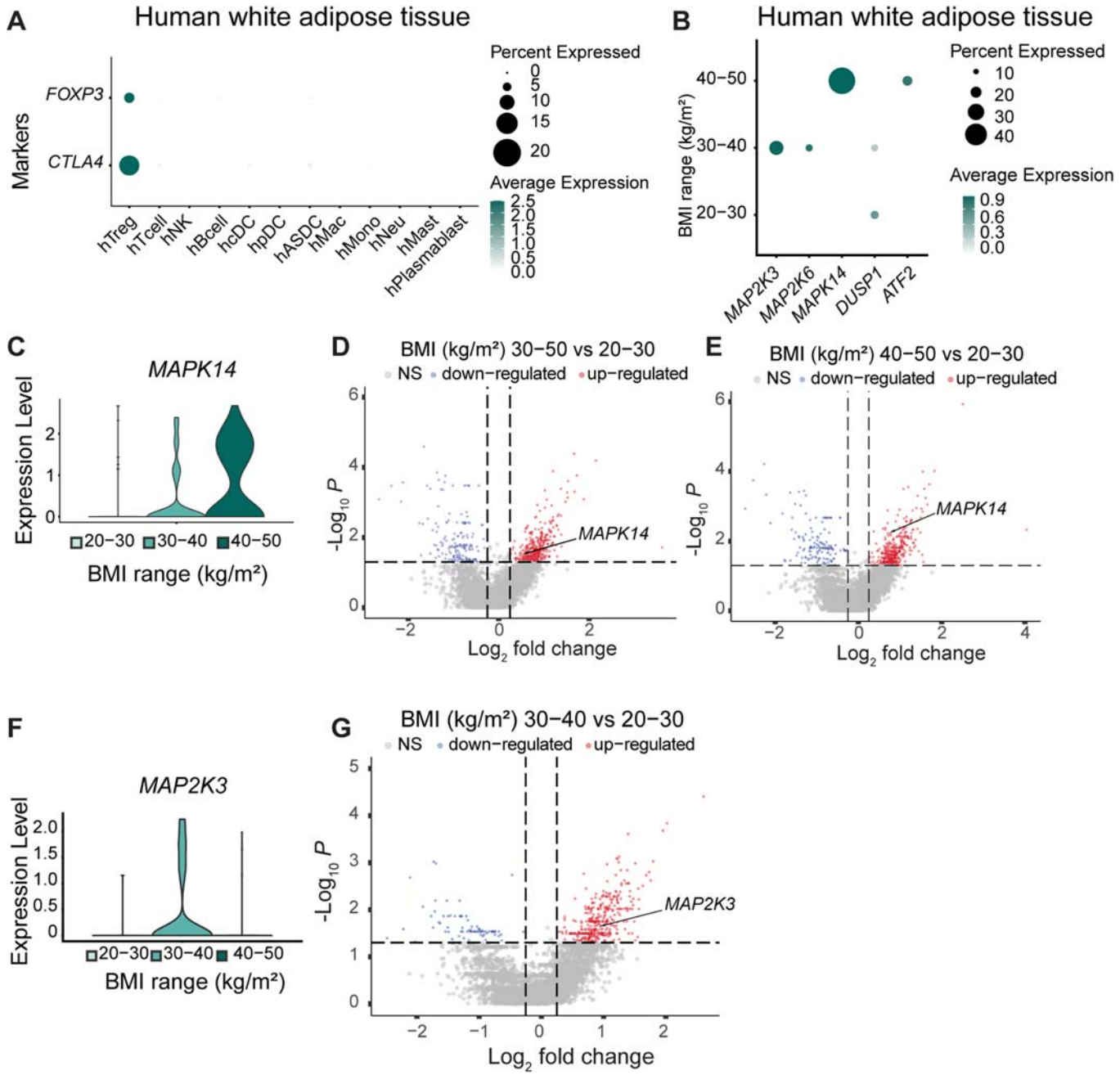

Figure EV5. p38 MAPK pathway is upregulated in Treg cells in obese human adipose tissue.

(**A–G**) The analysis was performed using human white adipose tissue single-cell RNA-seq data from Emont et al (Emont et al, 2022). (**A**) Dot plot of the expression of the indicated regulatory T cell (Treg) marker genes in the different cell type clusters. (**B**) Dot plot of the expression of the indicated genes by BMI range in human white adipose tissue Treg cluster shown in (**A**). (**C**) Violin plot showing the level of *MAPK14* gene expression by BMI range in the human white adipose tissue Treg dataset. (**D–E**) Volcano plots of differentially expressed genes in human white adipose tissue Treg subcluster in obese (BMI 30–40 kg/m^2) versus non-obese (BMI 20–30 kg/m^2) subjects (**D**) and in severe obese (BMI 40–50 kg/m^2) versus non-obese (BMI 20–30 kg/m^2) subjects (**E**). (**F**) Violin plot showing the level of *MAP2K3* gene expression by BMI range in the human white adipose tissue Treg dataset. (**G**) Volcano plots of differentially expressed genes in human white adipose tissue Treg subcluster in class 1 and 2 obesity (BMI 30–40 kg/m^2) versus non-obese (BMI 20–30 kg/m^2) subjects. The vertical dashed lines in (**D**, **E**, **G**) indicate a log2 fold change cut-off of 0.25. The horizontal dashed lines in (**D**, **E**, **G**) indicate a −log10 *p*-value cut-off of 1.3 (*p*-value < 0.05). Data information: Differentially expressed genes between BMI ranges were identified with a non-parametric Wilcoxon rank sum test. Obese (BMI 30–40 kg/m^2) $N = 3$ biologically independent patients; Severe obese (BMI 40–50 kg/m^2) $N = 6$ biologically independent patients; non-obese (BMI 20–30 kg/m^2) $N = 5$ biologically independent patients. DC: dendritic cells; Mac: macrophages; Mono: monocytes; Neu: neutrophiles; Mast: mastocytes.